

# A GBT SURVEY OF THE HALOGAS GALAXIES AND THEIR ENVIRONMENTS I: REVEALING THE FULL EXTENT OF HI AROUND NGC891, NGC925, NGC4414 & NGC4565

N. M. PINGEL<sup>1,2</sup>, D. J. PISANO<sup>1,2,3</sup>, G. HEALD<sup>4,5</sup>, T. H. JARRETT<sup>6</sup>, W. J. G. DE BLOK<sup>5,6,7</sup>, G. I. G. JÓZSA<sup>8,9,10</sup>, E. JÜTTE<sup>12</sup>, R. J. RAND<sup>13</sup>, T. OOSTERLOO<sup>5,7</sup>, AND B. WINKEL<sup>11</sup>

*Draft version May 27, 2022*

## ABSTRACT

We present initial results from a deep neutral hydrogen (HI) survey of the HALOGAS galaxy sample, which includes the spiral galaxies NGC891, NGC925, NGC4414, and NGC4565, performed with the Robert C. Byrd Green Bank Telescope (GBT). The resulting observations cover at least four deg<sup>2</sup> around these galaxies with an average  $5\sigma$  detection limit of  $1.2 \times 10^{18}$  cm<sup>-2</sup> over a velocity range of 20 km s<sup>-1</sup> and angular scale of 9.1'. In addition to detecting the same total flux as the GBT data, the spatial distribution of the GBT and original Westerbork Synthesis Radio Telescope (WSRT) data match well at equal spatial resolutions. The HI mass fraction below HI column densities of  $10^{19}$  cm<sup>-2</sup> is, on average, 2%. We discuss the possible origins of low column density HI of nearby spiral galaxies. The absence of a considerable amount of newly detected HI by the GBT indicates these galaxies do not have significant extended diffuse HI structures, and suggests future surveys planned with the SKA and its precursors must go *at least* as deep as  $10^{17}$  cm<sup>-2</sup> in column density to significantly increase the probability of detecting HI associated with the cosmic web and/or cold mode accretion.

*Keywords:* galaxies: evolution: galaxies: formation – galaxies: individual (NGC891, NGC925, NGC4414, NGC4565)

## 1. INTRODUCTION

Resolved neutral hydrogen (HI) observations undertaken over the past decade have revealed many intricate details related to the morphology and dynamics of spiral galaxies. A primary science goal of recent large surveys is to develop a deep understanding of how physical processes within the disks of spiral galaxies, such as star formation and the subsequent stellar feedback, affect their local circumgalactic environments. Surveys such as The HI Nearby Galaxy Survey (THINGS; Walter et al. 2008) and Hydrogen Accretion in LOcal GALaxies Sur-

vey (HALOGAS; Heald et al. 2011; hereby referred to as H11) performed with the Very Large Array (VLA) and Westerbork Synthesis Radio Telescope (WSRT), respectively, provide high resolution maps of the environments around nearby spiral galaxies.

Accretion of diffuse gas onto the disks of galaxies from the intergalactic medium (IGM) is a possible explanation for how the HI content of galaxies has remained relatively constant since  $z \sim 2$  while the star formation rate was up to 10 times higher at high redshifts (Noterdaeme et al. 2012; Madau & Dickinson 2014). The constant HI content implies that galaxies have somehow replenished themselves with enough gas to fuel continuous star formation. And though not directly responsible for star formation, HI is an intermediate phase towards molecular hydrogen, which is the raw ingredient of the star formation fuel. If the star formation is to continue, external gas has to be accreted and pass through the HI phase at some stage in the accretion process. Observationally inferred accretion rates as traced by HI, however, fall between 0.1 and  $0.2 M_{\odot}$  at low redshifts. This is a full order of magnitude lower than what is needed for galaxies to continually form stars at their current rates (Sancisi et al. 2008; Kauffmann et al. 2010). This discrepancy presents two intriguing scenarios: the cycle of star formation will eventually exhaust all of the available fuel within a few Gyr and star formation itself will gradually cease, or processes that refuel galaxies with the necessary gas have been missed by previous surveys. Numerical simulations have shown a likely mechanism for refueling star formation is through a quasi-spherical ‘hot’ mode and filamentary ‘cold’ mode (Kereš et al. 2005, 2009; Birnboim & Dekel 2003). Cold in the context of these numerical simulations refers to gas that has not been heated above the virial temperature of the galaxy’s potential well ( $\sim 10^5$  K), and hot refers to gas that has virialized in a process

<sup>1</sup> Department of Physics and Astronomy, West Virginia University, White Hall, Box 6315, Morgantown, WV 26506; nipingel@mix.wvu.edu

<sup>2</sup> Center for Gravitational Waves and Cosmology, West Virginia University, Chestnut Ridge Research Building, Morgantown, WV 26505

<sup>3</sup> Adjunct Astronomer at Green Bank Observatory, P.O. Box 2, Green Bank, WV 24944, USA.

<sup>4</sup> CSIRO Astronomy and Space Science, PO Box 1130, Bentley WA 6102, Australia

<sup>5</sup> Netherlands Institute for Radio Astronomy (ASTRON), Postbus 2, 7990 AA Dwingeloo, the Netherlands

<sup>6</sup> Department of Astronomy, University of Cape Town, Private Bag X3, Rondebosch 7701, South Africa

<sup>7</sup> Kapteyn Astronomical Institute, University of Groningen, PO Box 800, 9700 AV, Groningen, The Netherlands

<sup>8</sup> South African Radio Astronomy Observatory (SARAO), SKA South Africa, The Park, Park Road, Pinelands, 7405, South Africa

<sup>9</sup> Rhodes University, Radio Astronomy Research Group (RARG), PO Box 94, Grahamstown, 6140, South Africa

<sup>10</sup> Argelander-Institut für Astronomie, Auf dem Hügel 71, 53121 Bonn, Germany

<sup>11</sup> Max-Planck-Institut für Radioastronomie (MPIFR), Auf dem Hügel 69, 53121

<sup>12</sup> Astronomisches Institut Ruhr-Universität Bochum, Universitätsstraße 150, 44780 Bochum, Germany

<sup>13</sup> Department of Physics and Astronomy, University of New Mexico, Albuquerque, NM 87131, USA

akin to the classical theory of galaxy formation in which shock-heated, virialized gas with short cooling timescales accretes onto the central galaxy (e.g., Rees & Ostriker 1977). These simulations also suggest cold mode accretion was the dominant form of accretion at  $z \geq 1$  for all systems, and remains prevalent through  $z = 0$  for galaxies in low-density environments ( $n_{gal} \lesssim 1 \text{ h}^3 \text{ Mpc}^{-3}$ ) and  $M_{halo} \lesssim 10^{11.4} M_{\odot}$  (or  $M_{bary} \leq 10^{10.3} M_{\odot}$ ). For perspective, our own Milky Way has a virial (and thus halo) mass on the order of  $10^{12} M_{\odot}$ . These cold flows should exist in the form of vast filaments of cold, diffuse gas that permeate through the hot halo (Kereš et al. 2005). Comparisons by Nelson et al. (2013) between the smoothed particle hydrodynamic (SPH) numerical scheme employed in Kereš et al. (2005, 2009) and more sophisticated adaptive mesh refinement (AMR) simulations revealed the relative contribution of the cold mode is likely overestimated in earlier SPH simulations due to inherent numerical deficiencies. Nevertheless, the AMR simulations do show *some* fraction of gas is accreted cold.

The temperature of the gas in these predicted cold filaments is too high for a significant amount of neutral gas to exist within the largely ionized medium. However, AMR hydrodynamic simulations presented by Joung et al. (2012) show large amplitude non-linear perturbations can create cooling instabilities in which gas is collisionally excited and cools through subsequent radiative de-excitation of excited states. Large filamentary flows of inflowing gas are a possible seeding mechanism for non-linear perturbations, which allow gas to cool enough to form HI clouds within the inner most regions of the halo ( $R \leq 100 \text{ kpc}$ ) at HI column densities ( $N_{HI} \leq 10^{18} \text{ cm}^{-2}$ ) currently detectable with existing telescopes.

More recent independent ballistic models show galactic fountain activity can account for the presence of extraplanar HI around the Milky Way (in clouds like Complex C; Fraternali et al. 2015) and NGC891 (Fraternali & Binney 2006). In addition, Fraternali (2017) describes the condensation of hot coronal gas in the wake of the interaction with cooler galactic fountain gas, showing that fountain driven accretion can cool enough lower coronal gas to sufficiently extend the gas depletion time.

Observational evidence for predicted cold flows is very limited. Though absorption measurements, Stocke et al. (2010) and Ribaud et al. (2011) both find low metallicity gas infalling onto a nearby solar metallicity Lyman Limit System whose mass is consistent with the presence of cold flows predicted by simulations. The presence of infalling, low metallicity gas is certainly consistent with cold flows, but these measurements do not reveal any information about the extended spatial distribution of the accretion. Absorption measurements are very promising in that they accurately probe the metallicity of galaxy halos, but such studies require a quasar or other bright background source to measure the absorption line of interest. Absorption studies of the Milky Way, in which these desired sightlines are abundant, show our own Galaxy is surrounded by an immense amount of low column density gas that is both ionized and neutral (e.g., Wakker et al. 2003; Richter et al. 2017) with temperatures ranging from  $10^2$  to  $10^7 \text{ K}$ . Detection in emission does not rely on serendipitous sightlines required for ex-

ternal galaxies, and will constrain the large scale extent of the predicted cold flows or a potential diffuse component.

The unrivaled point source response of radio interferometers like the WSRT and VLA allows for incredible high resolution mapping capabilities at angular resolutions  $\sim \frac{\lambda}{b_{max}}$ , where  $b_{max}$  is the maximum baseline ( $b_{max} = 2.7 \text{ km}$  for the WSRT), which reveals the small scale structure of galaxies. On the downside, interferometers act as spatial filters by construction, and in particular due to the minimum possible spacing between neighboring telescopes in an interferometer (i.e., the physical size of each dish), there is a gap in  $u-v$  coverage at large angular scales from the absence of short baselines. This gap is often referred to as the ‘short-spacing’ problem, and it limits the amount of large scale structure an interferometer is able to detect (e.g., Braun & Walterbos 1985). As a consequence of the lack of sensitivity at large angular scales, past HI observations performed with interferometers may have missed significant reservoirs of gas around galaxies. On the other hand, the HI is observed in channels covering small velocity ranges only, and thus potentially does not extend enough to cause the sampled baselines to miss several interesting low-density, diffuse features. The full  $u-v$  coverage capability of single dish telescopes (Stanimirovic 2002) permits the detection of structure at all angular scales to test that notion. The unblocked aperture design of the GBT and resulting low sidelobes coupled with the compromise between resolution ( $9.1'$ ) and high surface brightness sensitivity ( $T_{sys} \lesssim 20 \text{ K}$ ) make it the ideal instrument to look for low column density structure around the HALOGAS sources.

The few surveys that have mapped down to  $N_{HI} \lesssim 10^{19} \text{ cm}^{-2}$  have uncovered several interesting low density, diffuse features. Perhaps most notably, Braun & Thilker (2004) discovered a low column density HI filament connecting M31 and M33. Two possible explanations for its origin have been presented since its discovery: either it is similar to filaments seen in simulations of the cosmic web (Popping et al. 2009), and thus an observational example of the cold mode accretion process, or it was created via a past tidal interaction between M31 and M33 (Bekki 2008; Putman et al. 2009). Higher resolution observations with the GBT by Wolfe et al. (2013) and Wolfe et al. (2016) show that this filament is clumpy in nature and made up of small HI clouds with  $M_{HI} \sim 10^{4-5} M_{\odot}$ ,  $N_{HI} \sim 10^{18} \text{ cm}^{-2}$ , and diameters on the order of kpc. M31 has a  $M_{dyn} \sim 1.3 \times 10^{12} M_{\odot}$  (Corbelli et al. 2010), which suggests the cold mode accretion scenario is unlikely. Furthermore, the total HI mass of these clouds is only  $4.6 \times 10^6 M_{\odot}$  providing only meager neutral mass accretion rates for a conservative infall time estimates of  $10^{7-8}$  years. The origin of these clouds is still an open and intriguing question which can be answered by utilizing sensitive observations of the HI within the circumgalactic environment of M31 and M33 (Wolfe et al. 2016).

Other recent detections by the GBT of large HI structures in NGC6946 by Pisano (2014) and NGC2403 by de Blok et al. (2014) suggest these features are seen around a variety of galaxies. In order to determine the true origin of these filaments, resolve the discrepancy between

observed accretion rates and SFRs, and obtain a comprehensive understanding of how the disks of galaxies interact with their surrounding circumgalactic environment, a comprehensive HI census spanning a wide range of astrophysically interesting properties (e.g., dynamical mass, total HI mass, halo mass, SFRs, etc) is required. A complete census of these properties will build up large number statistics and uncover any underlying correlations between intrinsic galaxy properties and possible signatures of accretion. The HALOGAS observations of 24 nearby galaxies obtained with the WSRT and the THINGS survey with the VLA are critical steps towards just such a census. To ensure this census is absolutely complete, interferometer observations must be supplemented with large single dish observations to cover all angular scales to assure large-scale emission is not resolved out by interferometers, and to map down to the lowest possible column density levels.

In this pilot paper we present data and analysis from four sources from the HALOGAS survey: NGC891, NGC925, NGC4414, and NGC4565. These GBT maps are among the deepest ( $N_{HI} \sim 10^{18} \text{ cm}^{-2}$ ) for external galaxies obtained to date in HI. This paper serves as an introduction to the full survey as a way to outline our analysis methods and highlight our overall goals. In Section 2 we present an overview of the HALOGAS sample; the observing configuration, reduction strategy and a discussion on our GBT beam model and how we convolve the WSRT data to avoid contamination from extended structure are outlined in Section 3. The results from our comparison between the GBT and WSRT data for our initial four sources are discussed in Section 4 with an investigation into how the diffuse HI environment relate to intrinsic galaxy properties following in Section 5. We then summarize our conclusions and commenting on future work in Section 6.

## 2. THE HALOGAS DATA AND SAMPLE

### 2.1. WSRT Data Cubes

The high-resolution HALOGAS cubes were produced from data obtained with the WSRT. See H11 for complete details on the observational configuration and data reduction of these data; see also Oosterloo et al. (2007) for configuration and reduction details specific to NGC891. A particular aspect of the HALOGAS observational setup we wish to highlight here is the minimum baseline length of 36 m, which translates to a maximum recoverable angular scale of  $\sim 20'$ . As mentioned in the Introduction, this particular angular scale is important because smooth emission extending above this limit will not be present in the WSRT data but fully observable by the GBT.

As will be discussed below, a significant portion of our analysis relies on convolved WSRT data convolved to the GBT resolution. Flux measurements from convolved data have the potential to be misleading as convolved emission will extend outside the original ‘clean’ boundaries used to produce the final interferometer cubes. Fully cleaned maps of array data are the sum of the restored clean components and residual map. Generally, only a portion of a map is cleaned, and thus, will have the correct flux. The flux in uncleaned portions of the map will be overestimated by a factor equal to the ratio of

the dirty beam size to clean beam size. We measure outside of the clean region because the convolution obviously extends source emission beyond its original boundaries. Including regions of uncleaned emission in the convolution will inevitably lead to misleading total flux measurements as pixels with uncleaned emission have an intensity scale defined as Jy per dirty beam as opposed to Jy per clean beam (e.g., Jorsater & van Moorsel 1995). In the interest of quantifying how the inclusion of unclean emission will affect the overall flux measurements in the convolved WSRT data, we extract two sub-maps from the original WSRT high-resolution NGC891 cubes that include a different number of pixels that were excluded from the cleaning as part of the data reduction. We then compare the total HI flux values after convolving these sub-maps as described in Section 3.2. Specifically,  $\sim 60\%$  of the first extracted subregion includes pixels that were part of the original clean region, while the remaining 40% of the pixels in this sub-map were excluded from the cleaning algorithm. In the second sub-map,  $\sim 90\%$  of the pixels were cleaned during data reduction, while the remaining 10% of the pixels were excluded from cleaning. We find the total flux measurements of these two sub-maps to be the same. This indicates that while some uncleaned emission — whether from pixels not inside the original clean region or simply low-level emission below the original clean threshold — is inevitably included, the total flux estimates are not significantly affected. That said, there are still systematic calibration uncertainties introduced by the specific treatment of the raw  $u-v$  visibilities to consider. A few examples are the removal of residual baseline structure, flagged/missing baselines, antenna shadowing, and different weighting schemes applied to the complex visibilities. We adopt an overall systematic flux uncertainty of 5% to encapsulate uncertainties related to how the WSRT data were processed.

### 2.2. Sample

The total HALOGAS sample consists of 24 unbarred and barred, nearby spirals that span a very diverse range of astrophysically significant properties such as star formation rates (SFRs), HI mass ( $M_{HI}$ ), stellar mass ( $M_*$ ), baryonic mass ( $M_{bary}$ ), etc. The sample also consists of galaxies with a wide range of environments.

We adopt the best distance values listed for each source in H11. Given that the ‘best’ distances were determined by taking the median measurements from well established methods (e.g., Cepheid and/or tip of the red giant branch, planetary-nebulae luminosity function, Tully-Fisher distances), we adopt a conservative 10% overall uncertainty for these distances. The SFRs for all galaxies mentioned in this work besides NGC4565 and NGC2997 (to be discussed in Section 5.2 in regards to similar GBT data of nearby galaxies) are computed utilizing data from the  $22\mu\text{m}$  band of the Wide-field Infrared Survey Explorer (WISE), a space based observatory deployed to map the entire sky in the infrared, along with far-ultraviolet (FUV) luminosity data from the Galaxy Evolution Explorer (GALEX; Gil de Paz et al. 2007). We follow the method outlined in Jarrett et al. (2013) to obtain an infrared SFR ( $\text{SFR}_{IR}$ ) that traces star formation obscured by dust with further calibrations derived by Cluver et al. (2014) for the same IR bands. Due to the difficulty of disentangling the relative contribution

from young and old stellar populations to various Polycyclic aromatic hydrocarbon emission bands near  $12\mu\text{m}$ , we chose to use the  $SFR_{IR}$  derived from the WISE  $22\mu\text{m}$  band. The SFR tracing UV photons associated with young massive stars is given as

$$\log_{10} \left( \frac{SFR_{FUV}}{M_{\odot} \text{ yr}^{-1}} \right) = \log_{10} \left( \frac{L_{FUV}}{L_{\odot}} \right) - 9.69, \quad (1)$$

and is derived from the calibrations of Buat et al. (2008, 2011). Jarrett et al. (2013) combine  $SFR_{IR}$  and  $SFR_{FUV}$  to estimate a total SFR using the form

$$SFR_{tot} = (1 - \eta)SFR_{IR} + SFR_{FUV}, \quad (2)$$

where  $\eta$  represents the fractional contribution to the total IR emission from dust reradiating energy injected from old stars; the value of  $0.17 \pm 0.1$  is adopted (Buat et al. 2011; Jarrett et al. 2013). In the case of NGC4565, the SFR is taken from the HALOGAS calculations in Heald et al. (2012) since no FUV luminosities were available for these sources through *GALEX*.

The  $3.4\mu\text{m}$  band of *WISE* effectively traces light from old stars resulting in a practical measure of the stellar mass. Jarrett et al. (2013) show a linear trend exists between *WISE* W1–W2 and W2–W3 color and stellar mass-to-light ratios ( $M/L$ ). By relating the *WISE* color to 2MASS  $K_s$  in-band luminosity, a  $M/L$  ratio can be derived from the  $K_s$  stellar mass relation of Zhu et al. (2010). This trend is further explored in Cluver et al. (2014), in which the W1–W2 color and stellar masses from the Galaxy And Mass Assembly (GAMA; Driver et al. 2009, 2011) survey are used for empirical calibration of the relationship. The best-fit for their sample including both passive and star-forming systems, but excluding known active galactic nuclei sources and *WISE* colors dominated by nuclear activity ( $W1-W2 \geq 0.8$ ), is

$$\log_{10} \left( \frac{M_*/M_{\odot}}{L_{W1}/L_{\odot}} \right) = -1.96 (W_{3.4\mu\text{m}} - W_{4.6\mu\text{m}}) - 0.03. \quad (3)$$

We adopt this relation to determine aggregate stellar masses for the HALOGAS sources. See Jarrett et al. (2013) and Cluver et al. (2014) for explicit details on the calculating of aggregate stellar masses utilizing *WISE* data. The adopted distance and SFRs from H11 are summarized in Table 1. See Table 2 in H11 for a complete summary of the targets’ properties and explanation for how certain target properties such as SFRs and distances were derived.

### 3. GBT OBSERVATIONS AND DATA REDUCTION AND LOW-RESOLUTION WSRT CUBES

#### 3.1. Observations and Data Reduction

Our GBT maps were made in a “basket-weave” fashion by scanning the telescope for  $2^{\circ}/3^{\circ}$  along constant lines of Right Ascension ( $\alpha_{J2000}$ ) and Declination ( $\delta_{J2000}$ ) to stitch together a final  $4\text{ deg}^2$  ( $9\text{ deg}^2$  for NGC925) image (Mangum et al. 2007). If potential cold flows exist, their visibility in HI depends on how close to the disk the relatively warm gas of the flow transitions to the HI phase. For the range of distances of the sources presented in this work, the angular span of  $2\text{ deg}$  corresponds to approximately  $315\text{ kpc} - 620\text{ kpc}$ , which are sufficient to

capture a majority of the virial volume. Each row or column is offset by  $3'$ , and each scan consisted of a total of 72 separate 5 s integrations that were dumped every  $100''$  to ensure Nyquist sampling. NGC891 and NGC925 were observed during January 2010 as part of the GBT project 10A-026, while NGC4565 and NGC4414 were observed during October 2013 and 2014 as part of GBT projects 13B-406 and 14B-293, respectively. We obtained an additional ten hours to map the inner  $2 \times 1\text{ deg}^2$  region of NGC891 as part of GBT project 16A-411. NGC925 and NGC4565 were observed with the GBT Spectrometer as the backend while the Versatile GBT Astronomical Spectrometer (VEGAS) was the backend used for the observations of NGC4414. The observations of NGC891 we present in this work combine the initial data from the GBT Spectrometer with the additional ten hours of data which utilized VEGAS as the backend. During each observation, the band was centered on the HI line at the redshifts of the sources. The observing bandwidth, frequency resolution, noise at the native velocity resolution, and other data properties are summarized in Table 1. Calibration during the observation was done by frequency switching  $-30.0\%$  ( $-23.4\%$  for observations with VEGAS as the backend) of the total bandwidth from the center frequency at a one second period, and each observation session included time on 3C48, 3C147, or 3C295 as primary flux calibrator in order to compute a  $T_{cal}$  value for the noise diode.  $T_{cal}$  values computed for the Spectrometer varied between 1.53 and 1.57 K for both XX and YY polarizations with remarkably low scatter on the mean values of 1.56 and 1.57 for over a period of several months ( $1\sigma \sim 0.01\text{ K}$ ). The exceptional stability in the  $T_{cal}$  values translate to an upper limit on the uncertainty in the relative flux calibration to  $< 1\%$  (more on the absolute calibration below). The computed  $T_{cal}$  values for observations performed with VEGAS as the backend showed a significant decrease in the stability. We compute the mean  $T_{cal}$  for VEGAS-only observations to be 1.41 K and 1.43 K for the YY and XX polarizations, respectively with a  $1\sigma$  uncertainty equal to 0.05 K for each. The increase scatter in the VEGAS  $T_{cal}$  was likely due to a crosstalk issue in the electronics of the backend that pushed the upper limit on the absolute flux calibration slightly upwards to 5%, including other systematics such as baseline removal and, to a lesser extent,  $T_{sys}$  variation. The crosstalk issue manifested itself by offsetting the relative power levels between the XX and YY polarizations. This issue was fixed by the time we obtained our new data on NGC891 and consequently only NGC4414 data are affected. To ensure the derived  $T_{cal}$  values for VEGAS did not affect our flux calibration, we observed each HALOGAS source that used VEGAS as the backend in the Fall of 2016 as part of GBT project GBT16B-393. These observations were done explicitly in position-switching mode where the GBT was centered on source for five minutes, and then moved two degrees in Right Ascension to obtain a five minute off spectrum. Comparing spatially overlapping integrations between our original VEGAS data and those from the deep pointing observations showed very good agreement within the noise when the polarizations are averaged to derive the Stokes I component. We are therefore confident that the data presented here are not significantly affected by the large variation in the  $T_{cal}$  values. We

Source	$\alpha^a$	$\delta^b$	Systemic Velocity [km s <sup>-1</sup> ]	Total Bandwidth [MHz]	$\Delta v$ [km s <sup>-1</sup> ] <sup>c</sup>	$\sigma$ [mK] <sup>d</sup>	$d_{best}$ [Mpc] <sup>e</sup>	SFR <sub>tot</sub> [ $M_{\odot}$ yr <sup>-1</sup> ] <sup>f</sup>
NGC891	02 <sup>h</sup> 22 <sup>m</sup> 33.4 <sup>s</sup>	42°20'57''	528±4	50.0	5.15	10	9.2±0.9	3.92±1.75
NGC925	02 <sup>h</sup> 27 <sup>m</sup> 16.9 <sup>s</sup>	33°34'45''	553±3	50.0	5.15	12	9.1±0.9	0.91±0.16
NGC4414	12 <sup>h</sup> 26 <sup>m</sup> 27.1 <sup>s</sup>	31°13'25''	716±6	23.4	5.15	13	18±2	3.45±1.58
NGC4565	12 <sup>h</sup> 36 <sup>m</sup> 20.8 <sup>s</sup>	25°59'16''	1230±5	50.0	5.15	15	11±1	0.67±0.10

**Table 1**  
Summary of Observations and Properties

<sup>a</sup>Right Ascension (J2000)

<sup>b</sup>Declination (J2000)

<sup>c</sup>Velocity Resolution

<sup>d</sup>final rms noise per velocity channel

<sup>e</sup>adopted distance from H11

<sup>f</sup>SFRs derived from WISE; value for NGC4565 taken from (Heald et al. 2012)

still adopt an overall 5% flux uncertainty as an upper limit to account for possible errors in bandpass calibration, interference, and errors in modeling atmospheric effects. Given that the WSRT observations largely used the same calibrator sources, we are also confident in the relative flux calibrations between the two data sets. We determine the gain to be 1.86 K Jy<sup>-1</sup> based on the computed  $T_{cal}$  values and an  $\sim 0.65$  aperture efficiency at 1420 MHz (Boothroyd et al. 2011). The typical system temperature of observations fell between 15 K and 20 K.

The frequency switched data were reduced using a custom GBTIDL<sup>1</sup> routine to calculate a source temperature of the form

$$T_{src} = T_{CAL} \cdot \frac{P_s - \langle P_{s,off} \rangle}{\langle P_{s,off} \rangle - P_{s,off}}, \quad (4)$$

where the quantities in brackets denote averages of four integrations from each edge of the map for a total of eight ‘off’ integrations to increase the signal-to-noise.  $P_s$  refers to average power of the CalOn (noise diode on) and CalOff (noise diode off) states — i.e.,  $(\text{CalOn} + \text{CalOff})/2$  — for a single integration in either the reference ( $s = 0$ ) or signal ( $s = 1$ ) bandpass switching state.  $P_{off}$  is therefore the arithmetic mean of the CalOn and CalOff states for the ‘off’ spectrum generated from the average of the eight edge integrations in the corresponding bandpass state. Additionally, the denominator represents the average difference between CalOn and CalOff states for the corresponding switching bandpass. Equation 4 therefore calibrates our frequency-switched data as if we had position switched data. Using the edge of the map as a reference position is an advantage because we are able to obtain a reference spectrum for each RA/Dec scan without sacrificing telescope time to slew off source. In the case of NGC925, emission from a companion source near the edge of our map forced us to use eight contiguous integrations on the opposite map edge as our ‘off’ position. The reference bandpass ( $s = 0$ ) is then shifted in frequency to match the signal bandpass ( $s = 1$ ) and arithmetically averaged to improve the noise by a factor of  $\sqrt{2}$ . We then fit a third order polynomial to the emission free regions of the spectra for all of our sources to remove baseline structure and any residual continuum sources leftover from our calibration procedure. In order to convert to units of  $T_A^*$  we assumed a constant zenith opacity appropriate for 21cm observations of 0.01 (Chynoweth et al. 2011). We manually flagged  $\leq 0.5\%$  of all integrations due to broadband radio frequency interference using a custom graphical flagging GBTIDL rou-

tine. Finally, we used a boxcar smoothing function to produce raw GBT spectra at a velocity resolution of 5.15 km s<sup>-1</sup>. See Wolfe et al. (2016) and the GBT technical memo Wolfe et al. (2015) for a more comprehensive discussion on the mapping sensitivity, data acquisition, and reduction.

These calibrated data were then converted to a format readable by AIPS using the IDLTOSDFITS<sup>2</sup> program and imported into AIPS where they were gridded into the final raw GBT data cubes using a convolution function of a Gaussian-tapered circular Bessel function (Mangum et al. 2007) within the task SDGRD.

### 3.2. Convolution of WSRT data

Accurate comparisons between high-resolution interferometer observations and single dish observations require the interferometer data to be smoothed to the resolution of the single-dish data set. Conventional analysis approximates the single-dish beam with a Gaussian smoothing function. While this is normally a good approximation, our goal of detecting low column density material around nearby galaxies requires a more comprehensive treatment since the Gaussian approximation for the single-dish beam does not take into account radiation coming into the near sidelobes and wings of the main beam. Since our sources are well separated from Galactic HI we are only concerned with emission originating from HI in and near our target galaxies.

In order to account for extended emission coming into the GBT’s innermost sidelobes, we construct a model beammap motivated from recent detailed simulations of the aperture illumination of the GBT at 1.4 GHz (Srikanth 2017; private communication) as part of an ongoing project to produce a measured map of the GBT power pattern. We derive the model by taking the square of the forward Fourier Transform of a simulated in-focus aperture radiation pattern. An example of our calculated beam model is shown in Figure 1 as a contoured 2D polar plot. The farthest sidelobes in this map extend out approximately 1.2° on the sky in radius between the  $-40$  and  $-50$  dB level. Interestingly, the innermost sidelobes *are not* symmetric. Boothroyd et al. (2011) has thoroughly mapped the all-sky response of the GBT beam out at the farthest sidelobes. But due to system saturation effects within 1° of the Sun, the nearest sidelobes, which are most susceptible to contamination from stray radiation in this work, were not able to be accurately mapped. The model presented in that paper (see their

<sup>1</sup> <http://gbtidl.nrao.edu/>

<sup>2</sup> Developed by Glen Langston of NRAO; documentation at <https://safe.nrao.edu/wiki/bin/view/GB/Data/IdlToSdfits>.

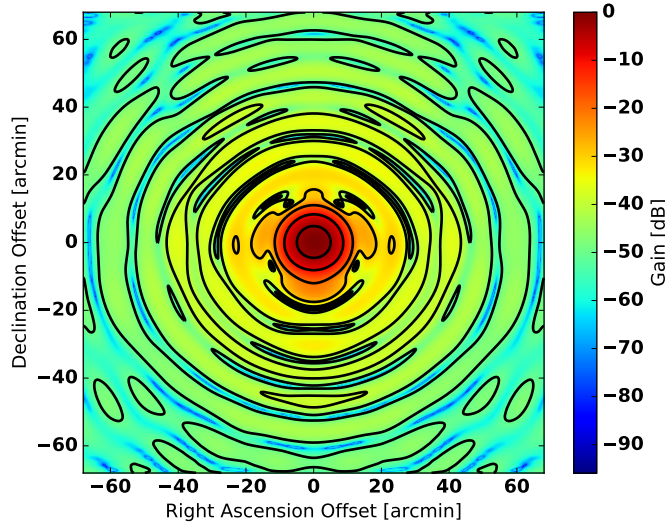


**Figure 1.** Normalized polar plot of a model GBT beam response on the sky. The contours represent dB levels of -3, -10, -20, -30, and -40.

Figure 5) showed the sidelobes were highly symmetric. Emission entering the sidelobes at  $\sim 1.2^\circ$  are not likely to contaminate our spectra as the gain here is approximately 50 dB down from the peak of the primary beam. However, the first sidelobe is only 30 dB down from the peak response. This makes contamination possible with some sources that have strong, extended emission out to  $\sim 0.5^\circ$ . We account for the possibility of contamination in the nearest sidelobes by using the GBT model beam map to include the sidelobe geometry in the convolution of the WSRT cubes. This provides the most accurate comparison possible between the two data sets without a genuine, measured beam map of the GBT.

There are, however, subtle consequences from utilizing a beam model with a set size as a smoothing kernel for high-resolution data. Namely, the final angular resolution of the convolved data will be *slightly* coarser than the GBT data because the high-resolution data are already convolved with the WSRT clean beam. Since the GBT beam model is not strictly Gaussian, we cannot solve for the optimal size of the kernel by taking the quadrature difference between the respective full-width half maximum (FWHM) values of the GBT and WSRT clean beam. We instead employ a Fourier Transform ( $\mathfrak{F}$ ) deconvolution method wherein the  $\mathfrak{F}$  of the GBT beam model ( $\mathfrak{F}[\Omega_{GBT}]$ ) is divided by the  $\mathfrak{F}$  of the WSRT clean beam ( $\mathfrak{F}[\Omega_{WSRT}]$ ) to derive an optimal smoothing kernel,  $K\{WSRT \rightarrow GBT\}$ .

We follow a similar procedure described in Aniano et al. (2011) to apply the necessary tapers that reduce numerical noise introduced by the FFT algorithm. We first taper the FT of the GBT beam with a piecewise function of the form

$$\Phi(k) = \begin{cases} 1 & \text{if } k < k_\alpha \\ \exp\left[-(1.8249 \times \left(\frac{k-k_\alpha}{k_\beta-k_\alpha}\right))\right] & \text{if } k_\alpha \leq k \leq k_\beta \\ 0 & \text{if } k_\beta < k \end{cases}$$

where  $k_\beta$  is taken to be the spatial frequency corresponding to four times the FWHM of the GBT and

$k_\alpha = 0.9k_\beta$ . We refer to the tapered form of  $\mathfrak{F}[\Omega_{GBT}]$  as  $\mathfrak{F}[\Omega_{GBT}]_\Phi$ . The amount of power removed from tapering the high spatial frequencies is much less than 1% since almost all of the power is contained near spatial frequencies corresponding to the main beam. Nevertheless, it is important to ensure high spatial frequencies are near zero to avoid introducing numerical artifacts when  $\mathfrak{F}[\Omega_{WSRT}]$  is divided out. We then take the reciprocal of  $\mathfrak{F}[\Omega_{WSRT}]$  and taper the result by the low-pass filter

$$f_T(k) = \begin{cases} 1 & \text{if } k < k_L \\ 0.5 \times \left[1 + \cos\left(\pi \times \frac{k-k_L}{k_H-k_L}\right)\right] & \text{if } k_L \leq k \leq k_H \\ 0 & \text{if } k_H < k. \end{cases}$$

Here  $k_H$  is chosen such that  $\mathfrak{F}[\Omega_{WSRT}](k_H) = 5 \times 10^{-3} \cdot \max(\mathfrak{F}[\Omega_{WSRT}])$  and  $k_L = 0.7 \times k_H$ . We choose  $k_H$  as such to ensure a high spatial frequency cutoff where  $\mathfrak{F}[\Omega_{WSRT}]$  is still appreciable, while the form of  $k_L$  is chosen to leave a majority of the lowest spatial frequency components unaffected by the filter.

The form of the optimal kernel is therefore given as

$$K\{WSRT \rightarrow GBT\} = \left| \mathfrak{F}^{-1} \left[ \mathfrak{F}[\Omega_{GBT}]_\Phi \times \frac{f_T}{\mathfrak{F}[\Omega_{WSRT}]} \right] \right|, \quad (5)$$

where  $|\mathfrak{F}^{-1}|$  represents the magnitude of the inverse Fourier Transform back to the sky plane. We note that Aniano et al. (2011) worked strictly with the real components since their kernels were largely rotationally symmetric. Since the WSRT clean beams are generally not symmetric, their Fourier Transforms will not be rotationally symmetric. As such, we work with the polar forms of  $\mathfrak{F}[\Omega_{WSRT}]$  and  $\mathfrak{F}[\Omega_{GBT}]$  to preserve the phase contribution. The resulting smoothing kernels are, as expected, *marginally* narrower than the GBT beam model with the largest residuals ( $\leq 0.01\%$ ) occurring towards the center.

### 3.3. Primary-beam Correction

The standard reduction techniques of imaging and deconvolution of interferometer data result in a model representation of the sky multiplied by the primary-beam

response of the antennas. The most accurate measure of flux requires a ‘primary-beam correction’ to the final data products, which we define as dividing out the primary-beam response of each velocity plane in the cube. We remove the primary-beam response from the native high-resolution WSRT cubes in the *Miriad* software package (Sault et al. 1995) with the same beam model used in H11. The primary-beam correction is applied before convolution as this most accurately represents the sky distribution observed by the interferometer. Furthermore, since the resulting low-resolution data cube must be scaled by the ratio of the GBT beam to the smaller WSRT synthesized beam to account for resolution differences when measuring the total flux, we found that removing the primary beam response after convolution does not conserve the total flux value computed for the high-resolution cube. To avoid issues with the non-uniform noise properties towards the edge, we extract a sub-cube such that all spatial scales fall within the half-power point of the WSRT primary beam for our subsequent analysis.

#### 4. RESULTS

##### 4.1. Summary of Analysis

In the following section, we present initial analysis for four (NGC891, NGC925, NGC4414, and NGC4565) of the 24 total sources in the HALOGAS sample. By analyzing HI at various angular resolution and sensitivities, the extent of HI environment of these galaxies between  $18 \lesssim \log_{10}(N_{HI}/\text{cm}^2) \lesssim 21$  can be fully characterized. Before discussing results for individual sources, we first summarize the steps of our analysis.

##### 4.1.1. Global HI Profiles and Noise

The flux as a function of velocity measured in the three data cubes is shown in each target’s respective subsection. We first use the *Miriad* task REGRID to regrid each GBT cube to be on the same angular and spectral scale as their WSRT counterpart. We estimate the noise properties within each respective cube,  $\sigma(x, y)$ , by fitting the negative half of a histogram whose pixels values were drawn from a region with no emission in all velocity channels (i.e., those with and without emission) with a Gaussian. We determine the  $1\sigma$  noise in the native, primary-beam corrected high-resolution WSRT data cubes to be between 100 and 150 mK, between 10 mK and 15 mK for the regridded GBT cubes, and between 5 and 10 mK for the convolved, primary-beam corrected WSRT cubes. These noise properties are summarized in the fourth column of Table 2

##### 4.1.2. $N_{HI}$ Images

Since we are mostly interested in the low column density environments of our sources, care must be taken to correctly scale the convolved data, distinguish signal from noise, as well as calculating associated uncertainties. We do this for the cumulative HI mass as a function of radius and  $N_{HI}$ .

To this end, we determine the gain to convert the convolved, primary-beam corrected WSRT cubes from Jy/Beam to brightness temperature in units of Kelvin using the equation

$$T_b = \frac{\lambda^2 S}{2k\Omega_a}. \quad (6)$$

Here  $S$  is the flux density,  $\Omega_a$  is the beam solid angle,  $k$  is the Boltzmann constant and  $\lambda$  is the wavelength of the observation (i.e., 0.211 meters). Taking these values and simplifying we arrive at

$$T_b [\text{K}] = \frac{6.87 \times 10^5 S [\text{Jy/beam}]}{\Omega_a [\text{arcseconds}^2]}. \quad (7)$$

The area of the GBT beam model used in this study is  $3.69 \times 10^5$  square arcseconds, while the area of the WSRT clean beam can be approximated as a Gaussian and is given by  $1.1331 \times (\theta_{maj} \cdot \theta_{min})$  (the major and minor axis in arcseconds, respectively). If one multiplies Equation 7 by the reciprocal of the flux density,  $S$ , and plugs in the area of the GBT beam model, it returns the gain factor of 1.86 [K/Jy] as derived in Section 3.1.

Computing the noise on an individual pixel basis is imperative to the treatment of the WSRT data (at both high and low resolutions) since the primary-beam correction changes the behavior of the noise as a function of position. The noise in the GBT data is relatively uniform over the cube, though the characterization of individual pixel noise is useful for constraining uncertainties in subsequent analysis. Since the original WSRT cubes were Hanning smoothed to their final velocity resolution, the pixels along the velocity axis are not independent. Verheijen & Sancisi (2001) show an associated  $1\sigma$  noise map can be computed by

$$\sigma_N(x, y) = \sqrt{\left(N(x, y) - \frac{3}{4}\right) \frac{4}{\sqrt{6}} \sigma(x, y)}, \quad (8)$$

where  $N(x, y)$  is the number of pixels used in the integration. For each data cube we produce masked (where emission below some threshold is blanked) and unmasked  $N_{HI}$  images. Masked images are useful when studying the radial dependence on column density since we wish to characterize the spatial variations of low-level signal, while unmasked images are used when studying the properties of the total flux.

We follow Verheijen & Sancisi (2001) and Lelli et al. (2014) by first constructing a mask for our high-resolution data by spatially smoothing the high-resolution cubes to  $40''$  ( $50''$  in the case of NGC4414) and only include pixels above  $3\sigma(x, y)$  — as determined from a fit to the negative half of a histogram — in the sum. As a consequence of this mask application, the number of channels used in the sum, and thus the uncertainty, will vary pixel-to-pixel in the resulting  $1\sigma$  noise maps. Due to the variation across the map, a global  $3\sigma$ -level is no longer straightforward to calculate. We calculate a global  $3\sigma$   $N_{HI}$ -level in these cubes by creating a signal-to-noise (S/N) map by taking the ratio of the masked  $N_{HI}$  images with the  $1\sigma$  noise maps. We then take the average of pixels in the S/N maps satisfying  $2.75 \leq \text{S/N} \leq 3.25$  to ensure a large enough sample to compute a reliable mean value. The final  $N_{HI}$  images only contain pixels whose value lies above this  $3\sigma$ -level. In the case of the low-resolution WSRT and GBT data, we repeat the masking procedure as described above but directly discard pixels which do not meet the  $3\sigma(x, y)$  threshold without constructing a spatially coarser cube. The beam sizes,  $\sigma(x, y)$  values,  $\sigma(x, y)$ , total flux, the  $N_{HI}$   $3\sigma$ -level, and velocity resolutions for the data sets



Source	$\theta_{maj}$ [arcseconds]	$\theta_{min}$ [arcseconds]	$\sigma$ [K]	S [Jy km s <sup>-1</sup> ]	$3\sigma N_{HI}$ [cm <sup>-2</sup> ]	$\Delta v$ [km s <sup>-1</sup> ]
<b>NGC891</b>						
High-Res WSRT	28.0	21.4	0.100	$(1.90 \pm 0.09) \times 10^2$	$6.7 \times 10^{19}$	8.24
Conv. WSRT	546.0	546.0	0.003	$(1.91 \pm 0.09) \times 10^2$	$2.0 \times 10^{18}$	8.24
Regridded GBT	546.0	546.0	0.010	$(1.93 \pm 0.09) \times 10^2$	$6.8 \times 10^{18}$	8.24
<b>NGC925</b>						
High-Res WSRT	37.9	33.2	0.130	$(2.85 \pm 0.14) \times 10^2$	$2.4 \times 10^{19}$	4.12
Conv. WSRT	546.0	546.0	0.003	$(2.84 \pm 0.14) \times 10^2$	$1.8 \times 10^{18}$	4.12
Regridded GBT	546.0	546.0	0.013	$(2.96 \pm 0.15) \times 10^2$	$4.0 \times 10^{18}$	4.12
<b>NGC4414</b>						
High-Res WSRT	39.0	33.5	0.130	$(6.2 \pm 0.3) \times 10^1$	$5.2 \times 10^{19}$	4.12
Conv. WSRT	546.0	546.0	0.005	$(6.1 \pm 0.3) \times 10^1$	$2.0 \times 10^{18}$	4.12
Regridded GBT	546.0	546.0	0.013	$(7.3 \pm 0.4) \times 10^1$	$5.2 \times 10^{18}$	4.12
<b>NGC4565</b>						
High-Res WSRT	33.5	30.8	0.150	$(2.74 \pm 0.14) \times 10^2$	$4.8 \times 10^{19}$	4.12
Conv. WSRT	546.0	546.0	0.004	$(2.71 \pm 0.14) \times 10^2$	$1.7 \times 10^{18}$	4.12
Regridded GBT	546.0	546.0	0.015	$(2.66 \pm 0.13) \times 10^2$	$7.0 \times 10^{18}$	4.12

**Table 2**  
Summary of Data Cubes

are summarized in Table 2.

#### 4.1.3. The Cumulative HI Mass vs. $N_{HI}$

Since HI mass is simply proportional to column density times a physical area, and we have the distance to each source, we can convert an individual pixel value of column density to an equivalent HI mass to determine the HI mass probability distribution function, which measures the total HI contained within discrete  $N_{HI}$  bins. Integrating this distribution therefore gives the *cumulative HI mass as function of  $N_{HI}$* , which measures the total HI mass for pixels equal to or exceeding  $N_{HI}$  bins. This distribution conveniently describes the fraction of HI mass above and below distinct  $N_{HI}$  thresholds. We can use the cumulative HI mass distribution as a diagnostic for how well the WSRT data recover the extended HI around these sources. For example, if the GBT data detected an extended diffuse HI feature that was resolved out by the WSRT, the cumulative HI mass distribution should deviate at lower column densities. In all cases presented here, the profiles flatten out well before the  $N_{HI}$   $3\sigma$ -level listed in Table 2. We set the lowest bin to be equal to one half the listed  $N_{HI}$  value in order to avoid the inclusion of noisy pixels and focus on the behavior between low and intermediate  $N_{HI}$  levels. The maximum bin size is set to 90% of the peak  $N_{HI}$  value. Note that the cumulative HI mass as a function of  $N_{HI}$  from both telescopes are normalized by the total GBT HI mass.

One aspect of concern when analyzing low-resolution data is whether emission adequately fills the larger GBT beam. In order to simulate the effect of this analysis on an unresolved source — where the low resolution map would simply trace the response of the GBT beam — we scale the GBT beam model introduced in Section 3.2 to the peak column density value of the GBT map and repeat the analysis calculating the cumulative HI mass as a function of  $N_{HI}$  (we do the same for the radial profiles of the of  $N_{HI}$  discussed in the next subsection). While the resolution effects will be source dependent, it is generally true that the large GBT beam does not hinder this (nor the radial average of  $N_{HI}$ ) analysis until the highest  $N_{HI}$  bins, which trace the structure of the main lobe.

#### 4.1.4. Radial Profiles of $N_{HI}$ and Cumulative Flux

The radial functions of the mean column density and cumulative flux are useful to compare how the properties of the HI emission detected by the GBT and WSRT change at various angular extents. For example, a large positive offset of cumulative flux and mean  $N_{HI}$  at large radii in the GBT data would indicate the WSRT resolved out large-scale HI emission. Additionally, profiles of the cumulative flux as a function of radius that do not flatten out or begin to dip at large radii may trace artifacts (e.g., negative bowls) in the high-resolution WSRT data. In the analysis of the radial extent of low column density structure, we use the masked  $N_{HI}$  images to ensure low-level signal has not been buried in the noise. The cumulative flux as a function of radius is derived from unmasked maps to best probe the radial variations in total flux. We also note that by measuring properties contained within radial bins overlaid on non-axisymmetric structure, the deviations at large radii inherently only reflect the distribution of HI along the major axis; thus, these plots do not reveal where potential differences between the maps occur. Nevertheless, any potential excess HI emission originating from structures spanning larger angular scales than what the WSRT is sensitive to should be evident even in radially averaged quantities. Finally, we note that no correction for inclination angle has been applied in the computation of these radial profiles. While the inclination of our sources range between  $\sim 50$  deg to  $\sim 90$  deg, we are most interested in the relative difference between the profiles derived between the GBT and WSRT data sets rather than how the radial properties change source-to-source. This relative offset between data sets for a particular source will be the unaffected by the correction factor of the cosine of the inclination angle.

As a further check of resolution effects, the solid black line in the radial column density profiles again denote the GBT beam model scaled to the peak  $N_{HI}$  value of the GBT data. Again, the model of an unresolved source deviates sufficiently well from the data indicating this analysis is not particularly hindered by resolution effects.

#### 4.2. NGC891

NGC891 is an edge on ( $i \gtrsim 89^\circ$ ) Sb/SBb galaxy whose HI has been extensively studied over the past two decades (e.g., Sancisi & Allen 1979; Rupen 1991; Swaters et al.



1997; Oosterloo et al. 2007). Utilizing the WSRT, Oosterloo et al. (2007) made deep, high-resolution maps of NGC891. These deep maps revealed a huge galactic halo containing 30% of the total HI mass. Other significant results from this study were: the discovery of a filament extending 22 kpc in projection from the disk towards the companion, UGC1807; counterrotating HI clouds in the halo; and differential rotation lagging with respect to the disk. Models of interactions between material from galactic fountain activity and hot coronal gas have successfully recreated the observed velocity rotational velocity gradient (Marinacci et al. 2010; Fraternali 2017). Halo pressure gradients and magnetic tension likely contribute as well (Benjamin 2002). See Figure 2 for the masked integrated HI image and velocity fields of NGC891 at low and high resolution. The GBT data do not reveal any low level emission extending from NGC891 to its companion, UGC1807.

The global flux density profiles for NGC891 derived from the GBT and WSRT data are shown in Figure 3a. There is excellent consistency between the profiles. The total measured flux for the GBT data is  $193 \pm 9$  Jy km  $s^{-1}$ . The flux density measured by the GBT translates to a total HI mass of  $(3.86 \pm 0.19) \times 10^9 M_{\odot}$  at the adopted distance of  $9.2 \pm 0.9$  Mpc from H11. The flux values for the convolved and high-resolution WSRT data are measured respectively to be  $191 \pm 9$  Jy km  $s^{-1}$  and  $190 \pm 9$  Jy km  $s^{-1}$ .

Figure 3b summarizes the results of the cumulative HI mass as a function of  $N_{HI}$  for NGC891. While the cumulated HI mass distribution from the simulated point source observation falls well below the data, values computed from the unmasked GBT and convolved WSRT  $N_{HI}$  images trace each other extremely well within the estimated uncertainties.

Figure 3c and d show the radial dependence of the mean column density and cumulative flux, respectively. The radial dependence of column density in the GBT and convolved WSRT data are effectively identical within 40 kpc, indicating the GBT data do not reveal any large-scale HI features (down to the HI column density sensitivity limit) that may potentially related to the substantial extraplanar HI component and filament observed in NGC891. In Figure 3d, the additional flux detected in the high-resolution WSRT data at projected scales smaller than the GBT beam (about 24 kpc at a distance of 9.2 Mpc) originates from emission that completely fills the smaller WSRT beam while remaining unresolved in the larger GBT beam. Past this point, all three data sets begin to converge to a similar value and profile shape. The dip in cumulative flux in the high-resolution profile highlights the presence of artifacts (e.g., a large-scale negative bowl caused by missing central baselines in the  $u-v$  coverage, or residual sidelobes leftover from the deconvolution of the dirty beam).

The channel maps in Figure 4 show the extent of the emission detected by the GBT at the  $5\sigma$  level traces the same  $5\sigma$  level in the WSRT data very well. Unlike similar GBT observations of NGC2403 (de Blok et al. 2014), another galaxy with a large HI filament, we do not detect any obvious structure associated with the 22 kpc long filament detected in the deep HI images presented by Oosterloo et al. (2007) in the individual channel maps. The agreement between the various data sets for NGC891

in total flux, mean column density as a function of radius, and the spatial extent of emission in the individual low-resolution data channel maps show the HALOGAS data do an excellent job at recovering the full HI distribution of NGC891; there is little difference between the HI environment at the  $N_{HI} \sim 10^{18} \text{cm}^{-2}$  as compared to the  $N_{HI} \sim 10^{19} \text{cm}^{-2}$  level.

### 4.3. NGC925

NGC925 is another galaxy within the HALOGAS survey whose HI distribution has been thoroughly studied over past decades (e.g., Gottesman 1980; Pisano et al. 1998; Walter et al. 2008; H11). For a galaxy such as NGC925, which has been observed as part of both THINGS and HALOGAS, we can compare the VLA, WSRT, and GBT observations. For this comparison, we utilize the same naturally weighted, residual scaled, blanked cube used to measure the total HI flux and moment maps in Walter et al. (2008) regridded to the WSRT spatial/spectral scale and convolved to the same angular resolution. Figure 5 shows two  $N_{HI}$  images (top and middle left) of NGC925 derived from GBT data. The expanded map shows the companion galaxy, UGC2023. There is no evidence for interacting or connecting material between NGC925 and UGC2023 seen in the GBT data. Figure 5 also shows a comparison between the WSRT-HALOGAS (middle right) and VLA-THINGS (top right) data for NGC925 in the form of  $N_{HI}$  images. It is clear that the more sensitive WSRT observations reveal a much more extended HI distribution than the THINGS data. This large structure  $\sim 26$  kpc across, which extends from  $\alpha_{J2000} = 02^h 24^m 30^s$ ,  $\delta_{J2000} = 33^{\circ} 17'$  to  $\alpha_{J2000} = 02^h 23^m 48^s$ ,  $\delta_{J2000} = 33^{\circ} 12'$ , is visible in the VLA THINGS data, albeit at very low levels. As the shortest baselines in the THINGS survey are effectively equal to those in HALOGAS at 35 m, we can attribute the additional structure observed by the WSRT strictly to a lower noise floor (as opposed to differences in the maximum recoverable angular scale). Figure 5 also shows the velocity field maps computed from the GBT (bottom left) and WSRT (bottom right) data with the contour levels are given in the Figure caption. The high resolution velocity field shows deviations from axial symmetry coincident with the disturbed structure in the  $N_{HI}$ , indicating a deviation from circular rotation. H11 attributes the origin to a possible interaction with a gas-rich dwarf companion seen as a faint enhancement in the Digital Sky Survey optical plates centered at about  $\alpha_{J2000} = 02^h 26^m 44^s$ ,  $\delta = 33^{\circ} 25' 20''$ .

We show the global HI profiles of NGC925 computed over the same angular area from the GBT, VLA, and the two WSRT data sets in Figure 6a. The GBT detects more flux over approaching velocities (approximately 430 km  $s^{-1}$  to 550 km  $s^{-1}$ ) than the WSRT, while both the WSRT and GBT detect more flux over the entire velocity range than what is measured in VLA data.

The difference in the profiles highlights that the recovered flux detected by an interferometer is dependent on the distribution and treatment (e.g., tapering of baseline amplitudes) of the complex visibilities. For this specific THINGS cube, the visibilities were ‘naturally’ weighted in the AIPS task IMAGR, meaning the visibilities were weighted to maximize surface brightness sensitivity. In the case of NGC925, the WSRT data were designed to

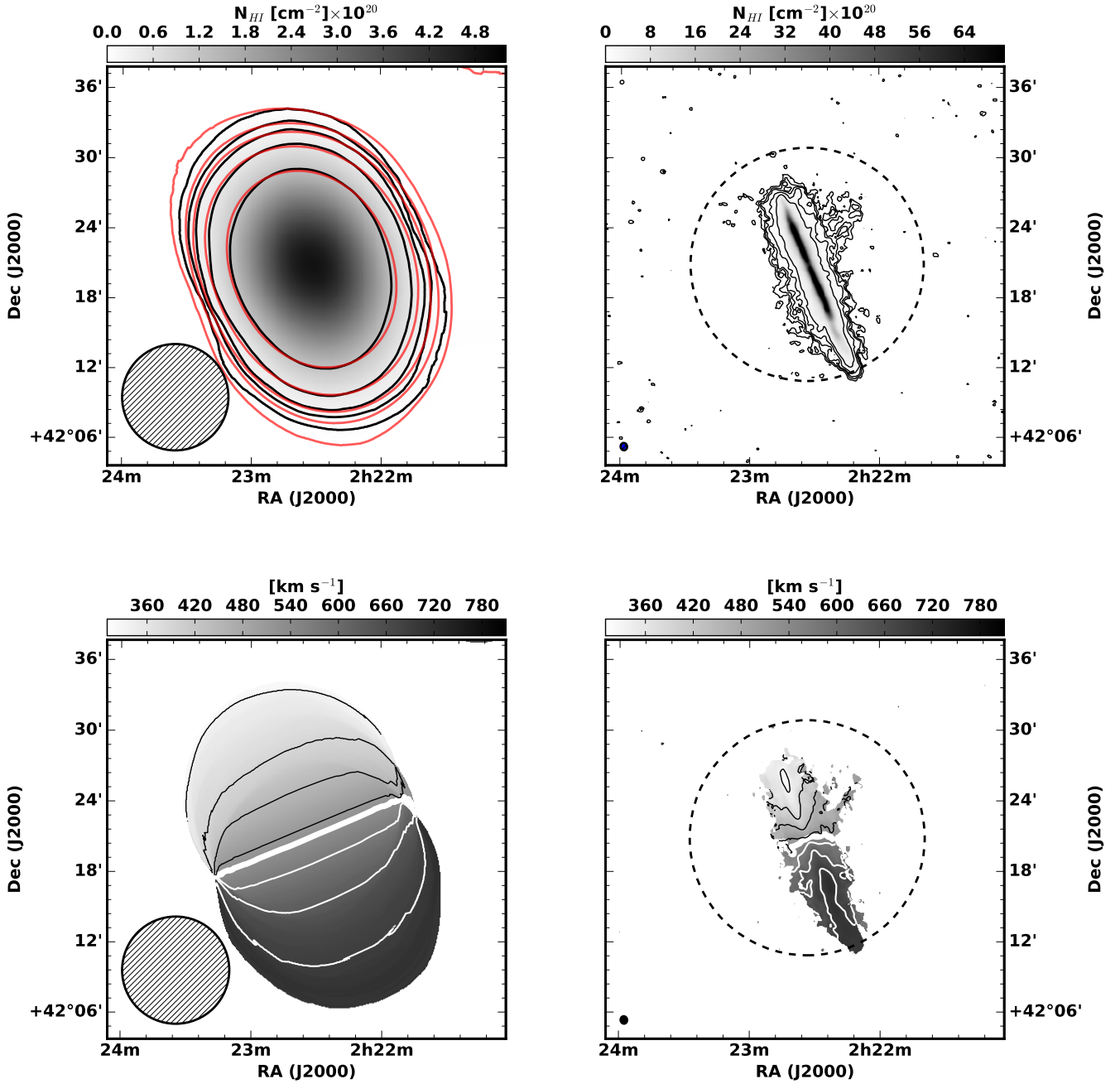


**Figure 2.** Integrated HI image (top) and velocity fields (bottom) for the low-resolution (left) and high-resolution WSRT (right) data for NGC891. The contours in the low-resolution  $N_{HI}$  images start at a column density value of  $5 \times 10^{18} \text{ cm}^{-2}$  and continue at 3, 5, 10, and 25 times that level. The black and red contours respectively denote the regridded GBT and convolved WSRT data. The contours in the associated high-resolution image begin at a level equivalent to  $2 \times 10^{19} \text{ cm}^{-2}$  and continue at 3, 5, 10, and 25 times that level. Note that the low-resolution velocity field is derived only from the GBT data cube. The contours in both velocity fields begin at  $330 \text{ km s}^{-1}$  and continue in steps of  $60 \text{ km s}^{-1}$ . The systemic velocity of  $528 \text{ km s}^{-1}$  is represented by the thick line, and the approaching and receding velocities are denoted by black and white contours, respectively. The dashed circles in the right two panels represent the maximum recoverable angular scale of the WSRT data.

maximize both sensitivity (natural – same weight) and control over the dirty beam (uniform – density) with the robust parameter set to 0 in the *Miriad* task, INVERT. An additional  $30''$  Gaussian taper was also applied to the higher spatial frequencies to further maximize sensitivity to faint extended emission. It is therefore a testament to the WSRT observations that approximately 20% more HI is detected as compared to the VLA data considering both were optimized to observe extended structure.

In addition to the differences in weighting schemes, the antenna positions between the VLA and WSRT cause immutable differences in  $u-v$  coverage making direct comparisons in terms of the total flux between these data sets impossible. We can therefore only conclude that, because of the agreement between both high and low-resolution WSRT and GBT flux profiles (which contains the zero-spacings information), there is excellent recovery of the diffuse HI in the WSRT-HALOGAS data for

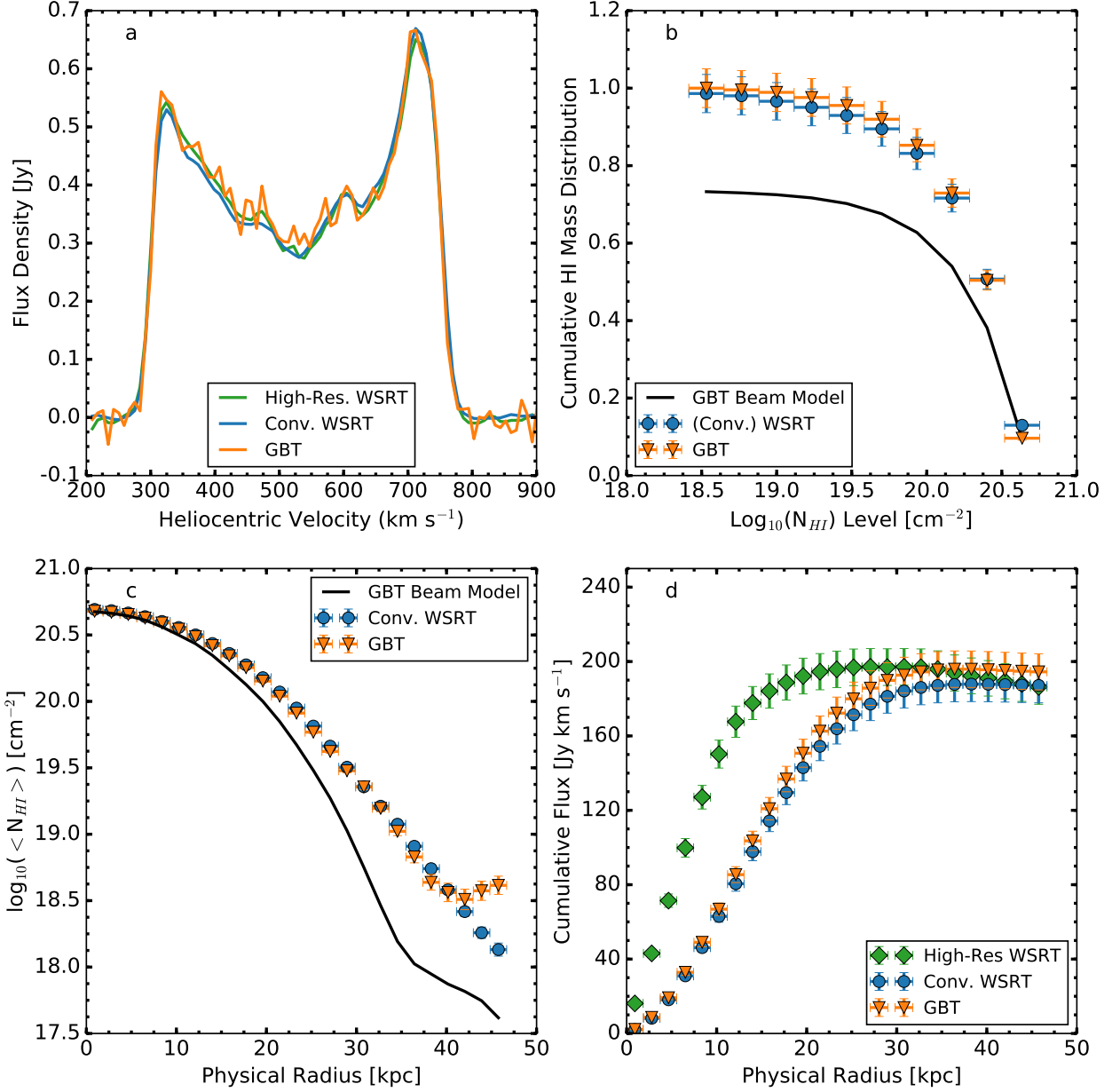


**Figure 3.** Comparison between the high-resolution (green diamonds) WSRT, convolved WSRT (blue circles), and regrided GBT (orange inverted triangles) data sets of NGC891. *a*: global HI profile; *b*: Cumulative HI mass as a function of  $N_{HI}$ . The solid black line simulates an unresolved observation with our GBT beam model; *c*: projected physical radial dependence on the azimuthally averaged  $N_{HI}$ ; *d*: projected radial dependence of the cumulative flux. In this case, we also show the results of our analysis on the high-resolution WSRT data.

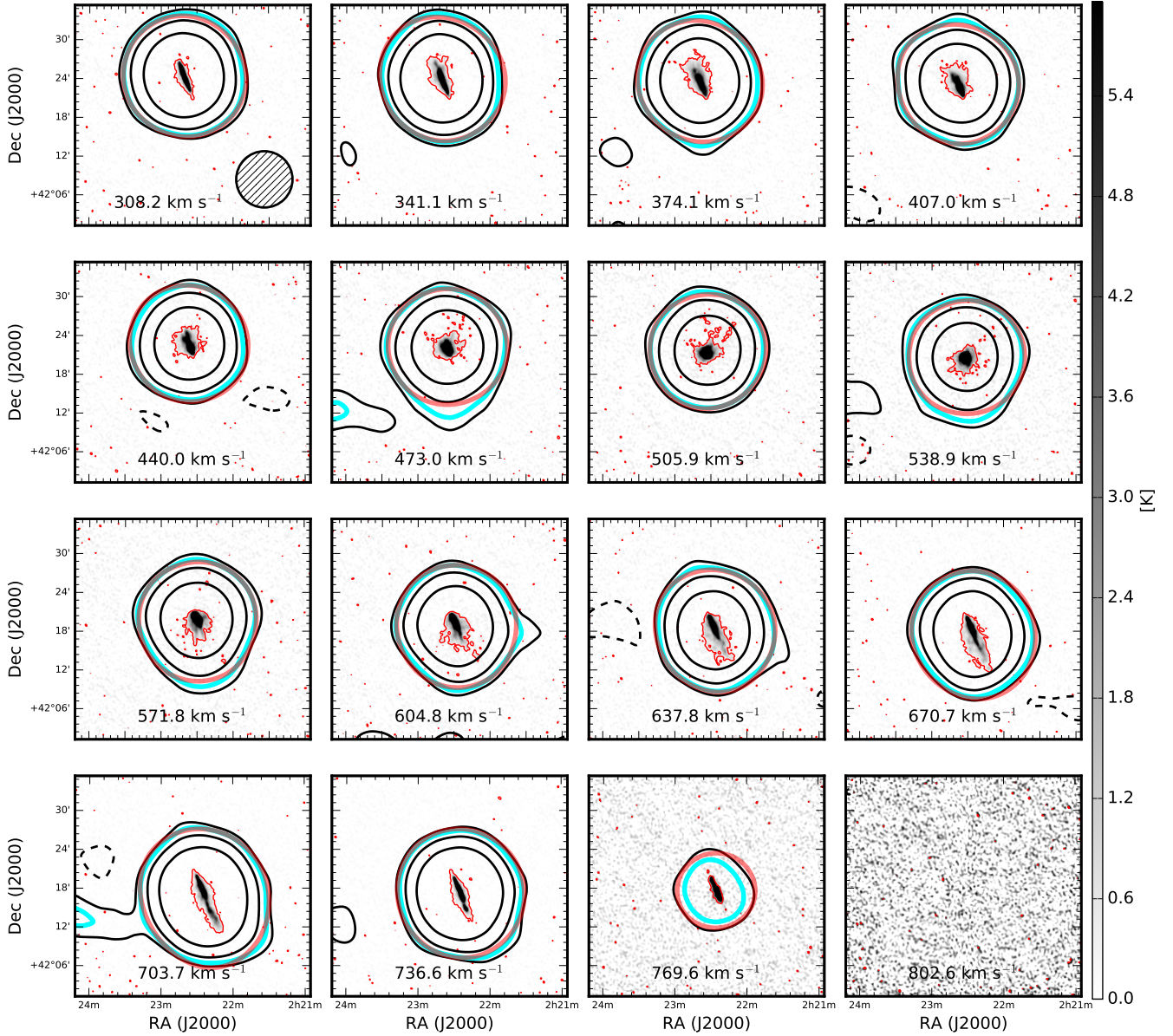


**Figure 4.** Selected channel maps of the NGC891 high-resolution WSRT data cube with corresponding GBT and convolved WSRT contours superimposed. The GBT data are shown in black and cyan contours at levels of -3 (dashed), 3, 5 (thick cyan), and 25 times 0.01 K, or equivalently a column density level of  $1.5 \times 10^{17} \text{ cm}^{-2}$  per  $8.24 \text{ km s}^{-1}$  velocity channel. The grey-scale shows the HI emission from the WSRT cube. The thin red line denotes a brightness temperature of 0.4 K, or a column density level of  $5.9 \times 10^{18} \text{ cm}^{-2}$ , and the thick red line denotes emission at  $7.5 \times 10^{17} \text{ cm}^{-2}$  (the same level of the cyan contour) in the primary-beam corrected WSRT cube convolved down to the GBT resolution. The GBT beam is shown in the top left panel.

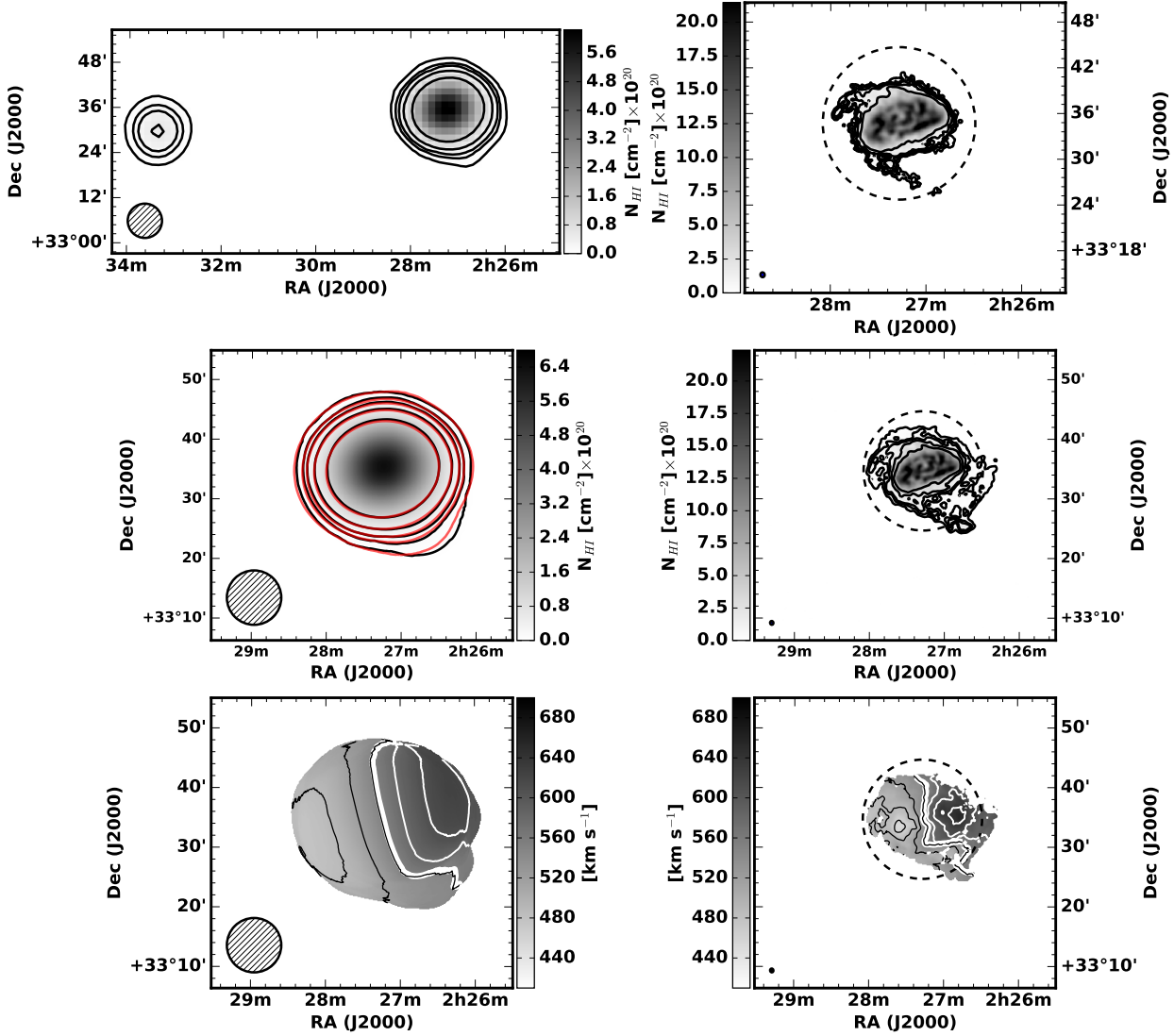


**Figure 5.** A comparison of several data sets for NGC925. The top left panel shows an integrated HI map of the GBT data for NGC925. UGC2023, a companion to the east of NGC925, is shown in the GBT map to highlight the absence of a diffuse HI bridge connecting the two galaxies. The top right panel shows an  $N_{HI}$  image computed from VLA-THINGS data. The middle and bottom left panels show a zoomed  $N_{HI}$  image of the low resolution cubes data and GBT velocity field. The middle and bottom right panels show the  $N_{HI}$  image derived from the WSRT data and associated velocity field. The red and black contours in the low resolution  $N_{HI}$  images respectively denote WSRT and GBT data; they begin at column density values of  $5.0 \times 10^{18} \text{ cm}^{-2}$  and continue at 3, 5, 10, and 25 times that level, while the contour levels in the VLA and WSRT  $N_{HI}$  images begin at a  $N_{HI}$  level equivalent to  $2.0 \times 10^{19} \text{ cm}^{-2}$  and continue at 3, 5, 10, and 25 times that level. The velocity field contours begin at  $430 \text{ km s}^{-1}$  and continue in steps of  $30 \text{ km s}^{-1}$ . The systemic velocity of  $553 \text{ km s}^{-1}$  is represented by the thick white line, and the approaching and receding velocities. The dashed circles in the right-hand panels represent the maximum recoverable angular scales of the WSRT and VLA data.

NGC925.

The cumulative HI mass as a function of  $N_{HI}$  for NGC925 is presented in Figure 6b. Just as is the case with NGC891, the cumulative HI mass as a function of  $N_{HI}$  measured by the GBT is traced reasonably well by the convolved WSRT data with only slight hints of excess HI in the  $N_{HI}$  bins below  $\log_{10}(N_{HI}/\text{cm}^2) = 20.5$ . The radial profiles of mean column density and cumulative flux also show consistency within the calculated uncertainties and expected behavior between the high resolution and convolved WSRT data. The slight decrease in the cumulative flux beginning at a projected physical radii 40 kpc also indicates the presence of a negative bowl in the WSRT data.

Selected channel maps of NGC925 from the WSRT-

HALOGAS data are shown in greyscale in Figure 7 with corresponding contours denoting emission from the GBT and convolved, primary-beam WSRT data overlaid. The GBT shows *slightly* more extended emission in some velocity channels. A majority of the slight extension corresponds to the velocity range of  $500\text{--}600 \text{ km s}^{-1}$  where the disturbed HI distribution seen in the high-resolution  $N_{HI}$  images of Figures 5 is most prevalent.

Our GBT observations detect  $(5.79 \pm 0.29) \times 10^9 M_{\odot}$  of HI, while the WSRT data reveal  $(5.54 \pm 0.28) \times 10^9 M_{\odot}$  of HI measured over the same angular area. H11 found faint emission extending towards the systemic velocity (see their Figure 6). This “beard” gas is interpreted as a slowly rotating halo seen in projection against the disk with a total HI mass on the order of  $10^8 M_{\odot}$ . While

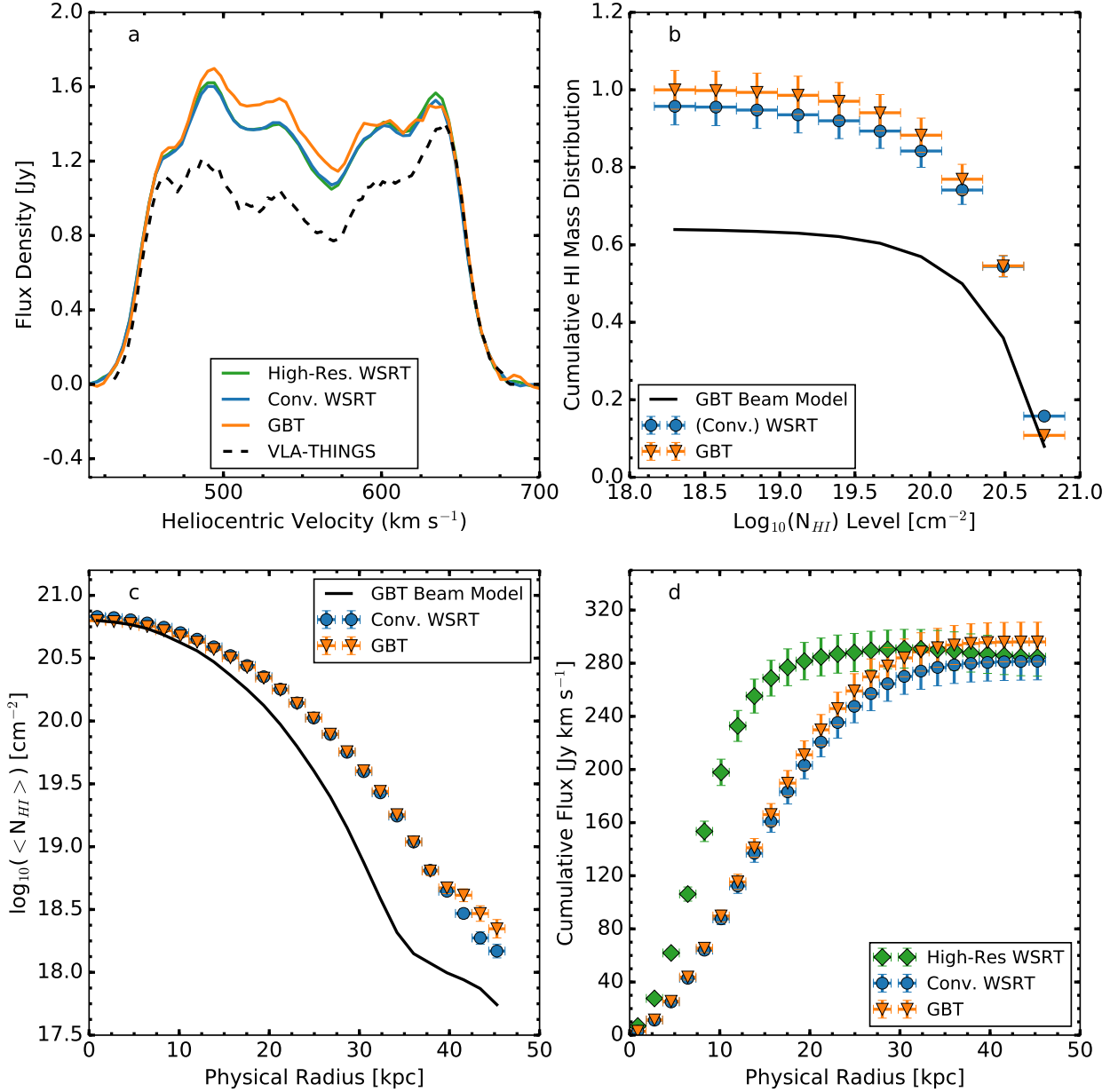


**Figure 6.** Comparison between the high-resolution (green diamonds) WSRT, convolved WSRT (blue circles), and regrided GBT (orange inverted triangles) data sets of NGC925. *a*: global HI profile; *b*: Cumulative HI mass as a function of  $N_{HI}$ . The dashed and solid black lines simulate the contribution of a Gaussian beam and our GBT beam model, respectively; *c*: projected physical radial dependence on the azimuthally averaged  $N_{HI}$ ; *d*: projected radial dependence of the cumulative flux. In this case, we also show the results of our analysis on the high-resolution WSRT data.



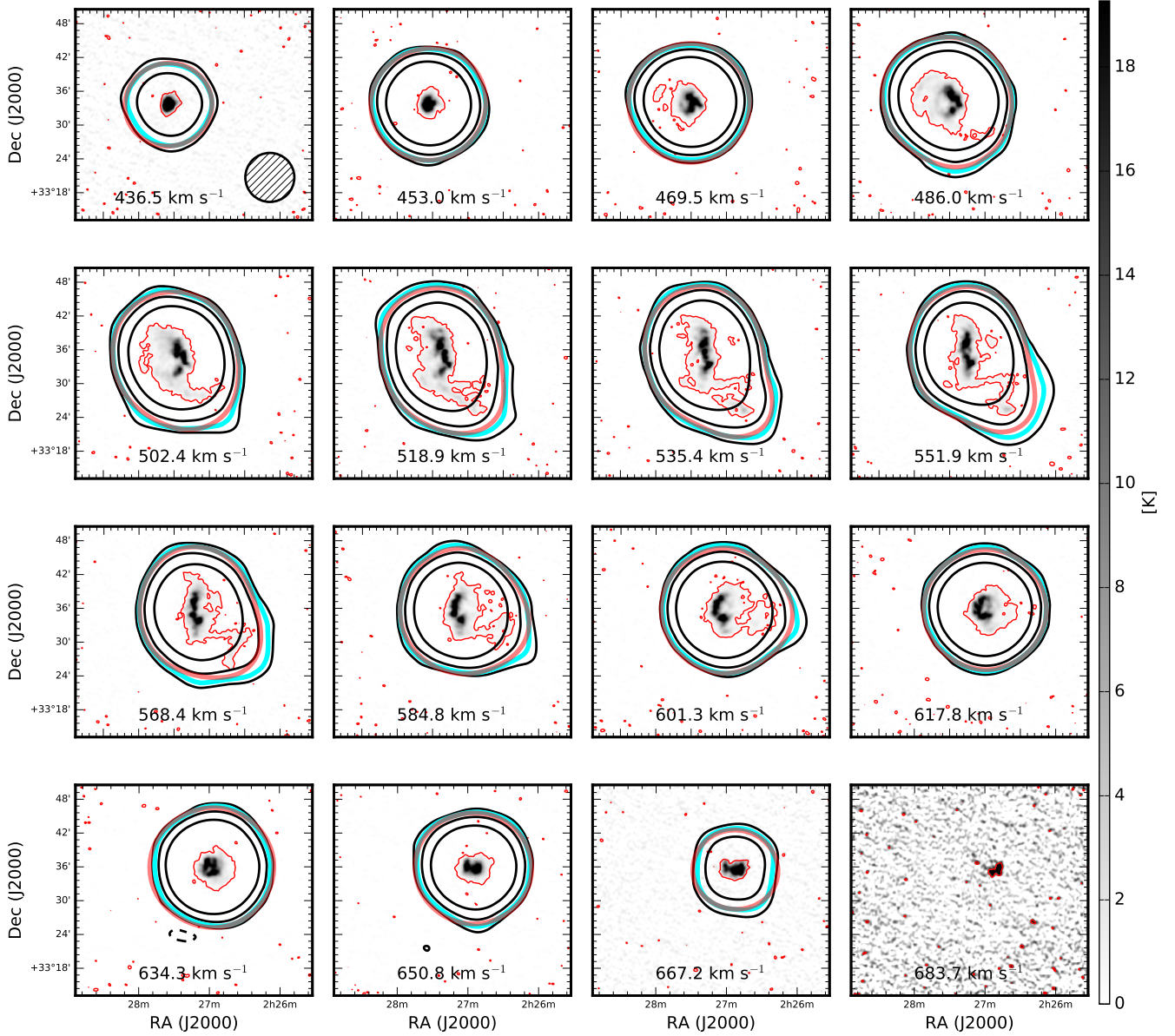


**Figure 7.** Selected channel maps of the NGC925 WSRT data cube with corresponding GBT channel maps superimposed. The GBT data are shown in black and cyan contours at levels of -3 (dashed), 3, 5 (thick cyan), and 25 times 0.01 K, or equivalently a column density level of  $9.75 \times 10^{16} \text{ cm}^{-2}$  per  $4.12 \text{ km s}^{-1}$  velocity channel. The grey-scale shows the HI emission from the WSRT cube. The thin red line denotes a brightness temperature of 0.36 K, or a column density levels at  $2.70 \times 10^{18} \text{ cm}^{-2}$ , and the thick red line denotes emission at  $4.88 \times 10^{18} \text{ cm}^{-2}$  (the same level of the cyan contour) in the primary-beam corrected WSRT cube convolved down to the GBT resolution. The GBT beam is shown in the top left panel.



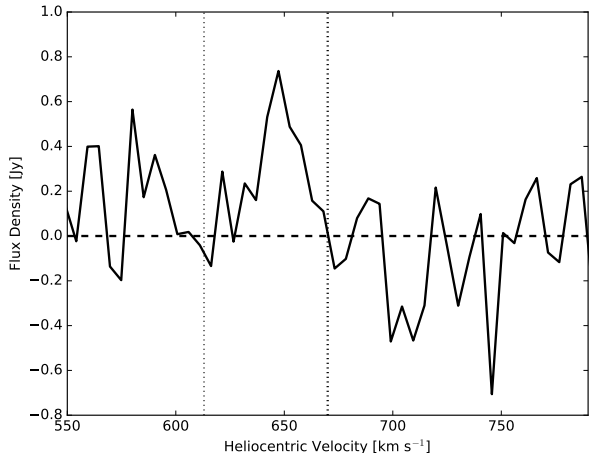


**Figure 8.** Global HI profile derived from GBT data for the northern companion of NGC925 deemed ‘Halogas’ by Karachentsev & Kaisina (2013).

slight in magnitude, there is some emission picked up by the GBT which was missed in the original HALOGAS observations. The GBT observations therefore reveal additional HI in NGC925 that must be some combination of extended and diffuse as it was not detected in neither optimally weighted VLA data nor in the more sensitive WSRT data. We defer correcting the WSRT data for missing short spacings for a future paper; nevertheless, a high-resolution cube that recovers emission at angular scales will provide an excellent data set for a detailed dynamical study relating the beard gas to the extraplanar component.

H11 also noted the presence of the a small companion centered to the North at about  $\alpha_{J2000}=02^h27^m20^s$ ,  $\delta=33^\circ57'30''$  in the velocity range of 613-665 km s<sup>-1</sup>. This companion was cataloged as ‘Halogas’ by Karachentsev & Kaisina (2013). The companion has a total HI mass (as measured by the GBT) of  $(3.11\pm0.15)\times10^7 M_\odot$  consistent with the measurement from H11. A global HI profile taken from the GBT data is shown in Figure 8; there is no detection of a bridge of HI between Halogas and NGC925.

#### 4.4. NGC4414

NGC4414 is a moderately inclined ( $i = 50^\circ$ ) SAc galaxy, and is one of the most distant galaxies in the HALOGAS survey at  $18\pm2$  Mpc. NGC4414 was characterized through tilted ring fitting (de Blok et al. 2014) as having a regular rotating inner disk within  $240''$  ( $\sim 21$  kpc at the distance of NGC4414) in radius and an outer disk that is mostly dominated by rotation with some evidence for radial and noncircular motions towards the edge of the extended HI distribution. The high-resolution WSRT-HALOGAS observations do not show any evidence for an interaction besides the disturbed outer disk, though NGC4414 likely has undergone some weak interaction with neighboring galaxies within the Coma I cluster in the past. de Blok et al. (2014) mention a possible source of an interaction may be the small galaxy, SDSS J122646.27+311904.8, but neither the WSRT or GBT detect any HI at its position.

A comparison between the GBT and WSRT data is

shown in Figure 9 in the form of integrated HI intensity and velocity field maps. As noted by de Blok et al. (2014), the inner regions of the velocity field show very well-behaved rotation in the inner regions of the galaxy with motions deviating from circular towards the edge of the HI disk. These areas of irregular rotation overlap well with the presence of the disturbed structure seen in the high resolution high-resolution WSRT  $N_{HI}$  image, which again, may be evidence for a past interaction. The extent of the overall HI distribution is within the maximum recoverable angular scale as denoted by the dashed circles.

The global flux density profiles of NGC4414 derived from the GBT and WSRT data are shown in the top left panel of Figure 10. The GBT detects more flux overall, and excess flux is encountered over almost the entire velocity range. The total HI mass measured by the GBT is  $(5.43\pm0.27)\times10^9 M_\odot$ , which is  $\sim 1\times10^9 M_\odot$  more HI than is measured in the WSRT data over the same area. The large offset in the fluxes may be due, in part, to a large plume of HI extension to the West, which is further evidence for a past interaction.

The cumulative HI mass as a functions of  $N_{HI}$  calculated from both data sets for NGC4414 are summarized in the top right panel. The convolved WSRT data begin to trace the simulated unresolved observation quite well past  $\log_{10}(N_{HI}/\text{cm}^2) = 19.0$ . The offset of  $\sim 15\%$  between the two data profiles at the lower  $N_{HI}$  bins indicates that the WSRT observations may resolve out structure that extends past the maximum recoverable angular scale with a peak  $N_{HI}$  on the order of  $\sim 10^{18} \text{ cm}^{-2}$ .

The radial dependent properties are shown in the lower two panels of Figure 10. The azimuthally averaged  $N_{HI}$  profiles interestingly begin to differ at projected physical of about 60 kpc, while a prevalent dip in the cumulative flux profiles of the WSRT data begins near 45 kpc. Considering the  $N_{HI}$  profiles are derived from masked  $N_{HI}$  images, the deviation between the GBT and WSRT profiles could reflect the presence of artifacts, such as leftover residual sidelobes from deconvolution, that increase noise properties at larger angular extents to mimic the presence of legitimate signal. The variations in the WSRT cumulative flux profiles explicitly demonstrate the presence of artifacts in these data cubes.

Channel maps of NGC4414 similar to Figures 4 and 7 are presented in Figure 11. The outermost  $3\sigma$  contour generally extends past the  $5\sigma$  contour of the convolved WSRT data in each selected velocity channel. This is consistent with the behavior of the global HI profile from Figure 10. The channel maps reveal the extent of the NGC4414 emission in a single velocity channel is within the angular sensitivity limit ( $\sim 20''$ , or  $\sim 100$  kpc at the distance of NGC4414) in the WSRT data. Additionally, the angular extent of NGC4414 is only a few times the GBT beam area as evidence by the steep drop in the cumulative HI mass function. Considering all these factors, we conclude that a majority of the excess emission detected by the GBT is likely due to artifacts (e.g., residual sidelobe structure) in the WSRT cubes, as opposed to resolved out structure.

de Blok et al. (2014) noted in their analysis that gas at velocities lower than the local rotational velocity (i.e., ‘beard’ gas) is present in both the receding and approaching sides of the rotation curve for the inner disk

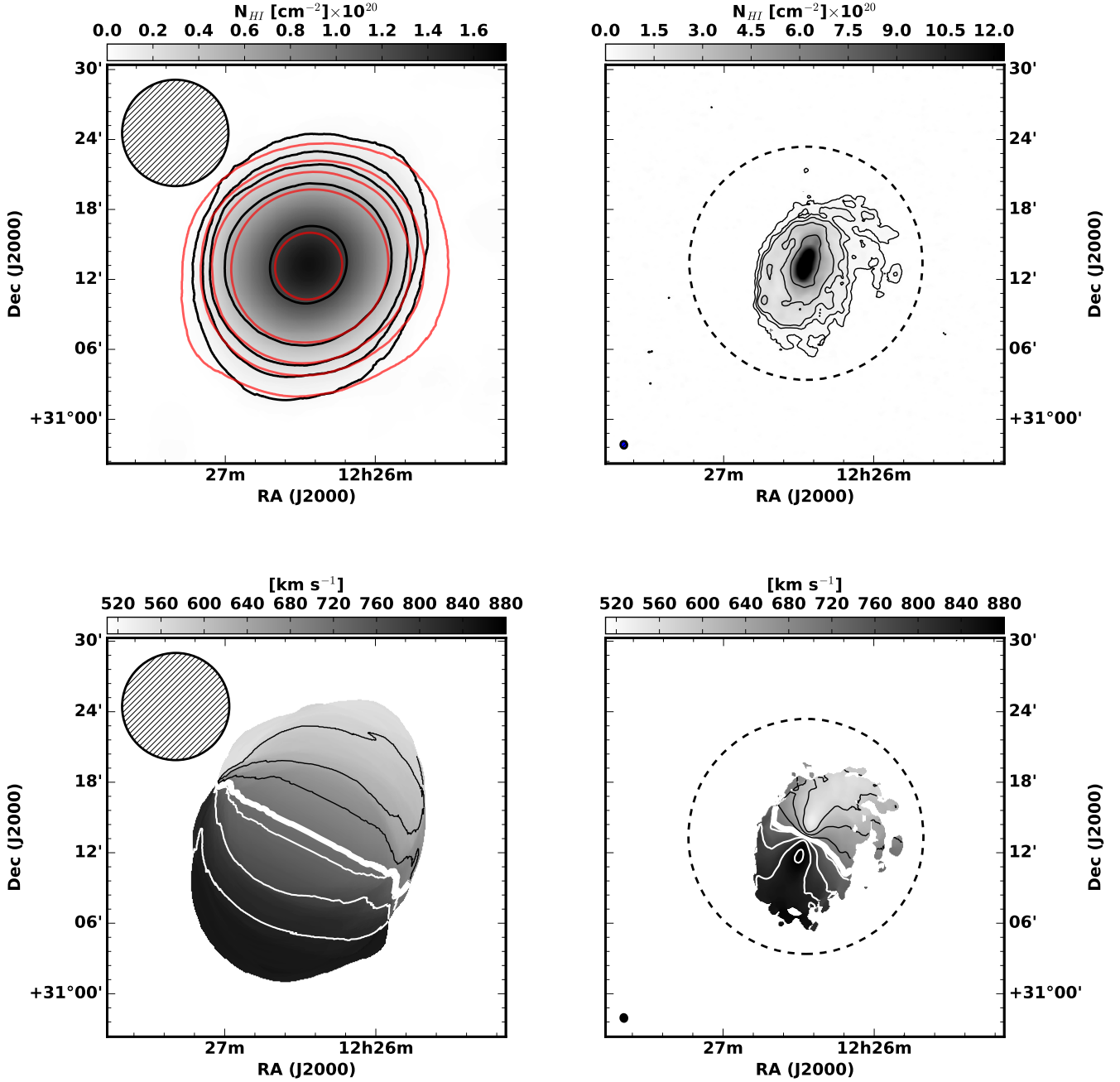


**Figure 9.** A comparison of the  $N_{HI}$  images (top) and velocity fields (bottom) of NGC4414 derived from the GBT (left) and WSRT-HALOGAS (right) data. The red and black contours in the low resolution  $N_{HI}$  images respectively denote WSRT and GBT data; they begin at a  $N_{HI}$  level of  $5.0 \times 10^{18} \text{ cm}^{-2}$  and increase by factors of 3, 5, 10, and 25. The contours in the high-resolution WSRT  $N_{HI}$  image begin at a  $N_{HI}$  level of  $2.0 \times 10^{19} \text{ cm}^{-2}$  and increase by factors of 3, 5, 10, and 25. The velocity contours in both maps begin at  $530 \text{ km s}^{-1}$  and increase by  $50 \text{ km s}^{-1}$  with the systemic velocity of NGC4414 of  $716 \text{ km s}^{-1}$  represented by the thick white contour. The receding and approaching sides are denoted by white and black contours, respectively. The GBT (WSRT) beams are shown for their respective data sets in the top (bottom) left corner of each panel. The dashed circles in the right-hand panels represent the maximum recoverable angular scales of the WSRT data.

of NGC4414, and should be interpreted as extraplanar gas in the inner disk. Through a variety of techniques including blanking high column density pixels and subtracting Gaussian fits of the velocity profiles within the observed data cube (Fraternali et al. 2002), de Blok et al. (2014) determined the HI mass of the extraplanar gas associated with the inner disk to be between 2 and 6.5 percent of the total HI mass of the inner disk (i.e., about  $2 \times 10^8 M_{\odot}$ ). Similarly, the authors concluded the extra-

planar gas associated with the outer disk to be about 1 to 2 percent of the total HI mass of the system. In the future, merging the GBT and WSRT data sets will provide an excellent basis for characterizing dynamical links between anomalous velocity gas and an extraplanar component in NGC4414 as well as characterizing the kinematics of a potential past interaction.

#### 4.5. NGC4565

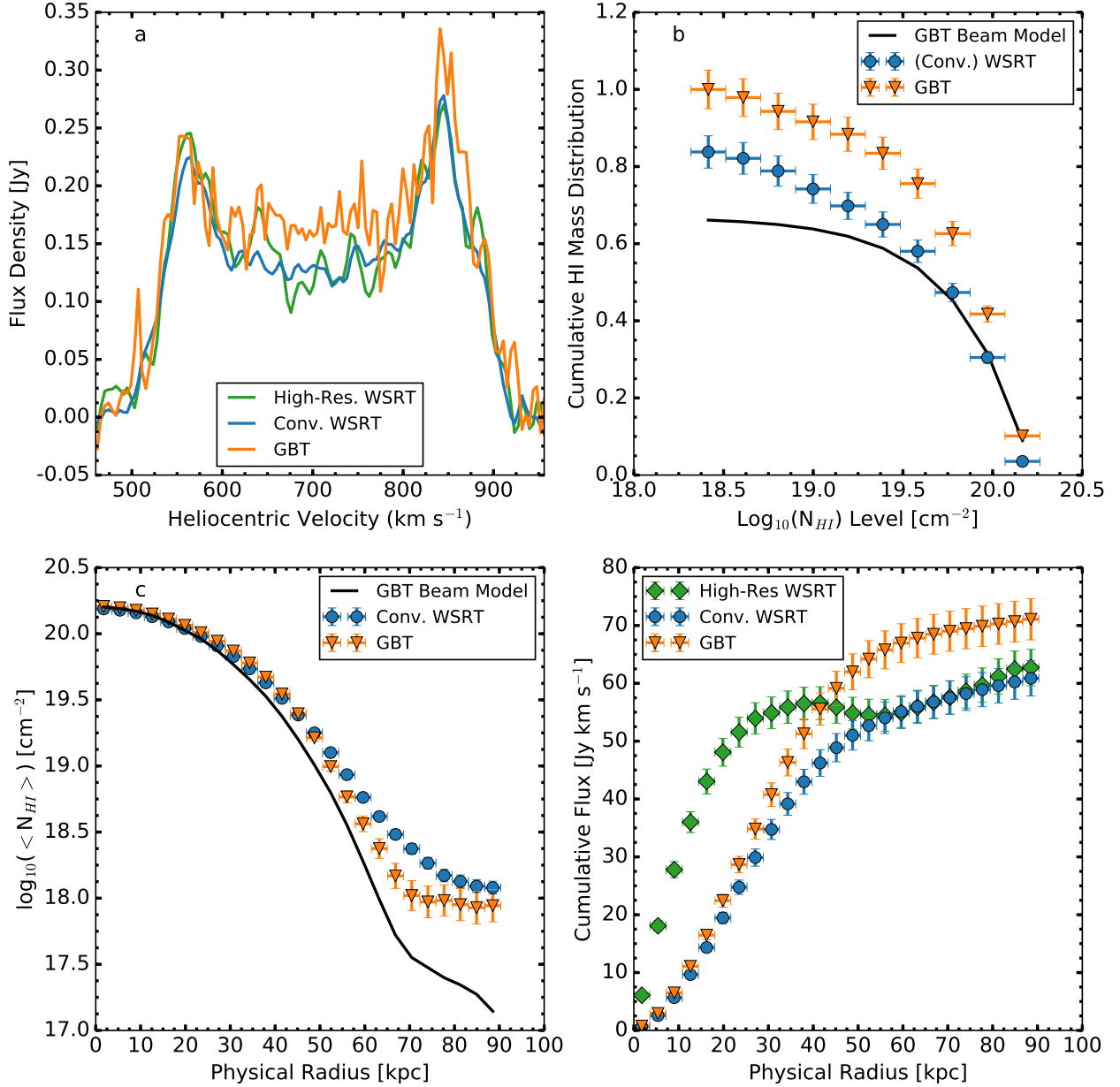


**Figure 10.** Comparison between the high-resolution (green diamonds) WSRT, convolved WSRT (blue circles), and regrided GBT (orange inverted triangles) for NGC4414. *a*: global HI profile; *b*: Cumulative HI as a function of  $N_{HI}$ . The dashed and solid black lines simulate the contribution of a Gaussian beam and our GBT beam model, respectively; *c*: projected physical radial dependence of the azimuthally averaged  $N_{HI}$ ; *d*: projected radial dependence of the cumulative flux. In this case, we also show the results of our analysis on the high-resolution WSRT data.

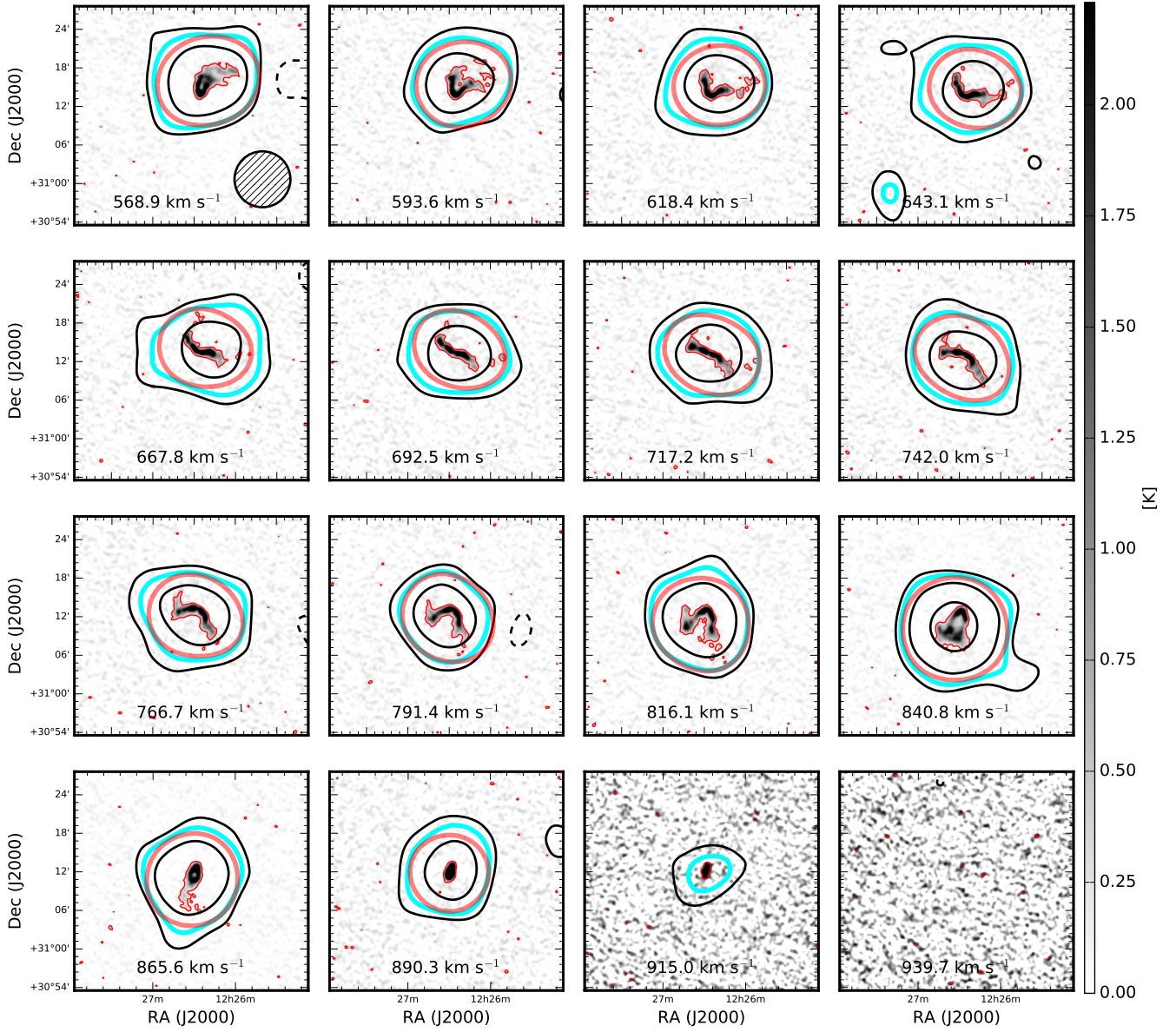


**Figure 11.** Selected channel maps of the NGC4414 WSRT data cube with corresponding GBT channel maps superimposed. The GBT data are shown in black and cyan contours at levels of -3 (dashed), 3, 5 (thick cyan), and 25 times 0.01 K, or equivalently a column density level of  $9.75 \times 10^{16} \text{ cm}^{-2}$  per  $4.12 \text{ km s}^{-1}$  velocity channel. The grey-scale shows the HI emission from the WSRT cube. The thin red line denotes a brightness temperature of 0.39 K, or a column density levels at  $2.92 \times 10^{18} \text{ cm}^{-2}$ , and the thick red line denotes emission at  $2.93 \times 10^{17} \text{ cm}^{-2}$  (the same level of the cyan contour) in the primary-beam corrected WSRT cube convolved down to the GBT resolution. The GBT beam is shown in the top left panel.

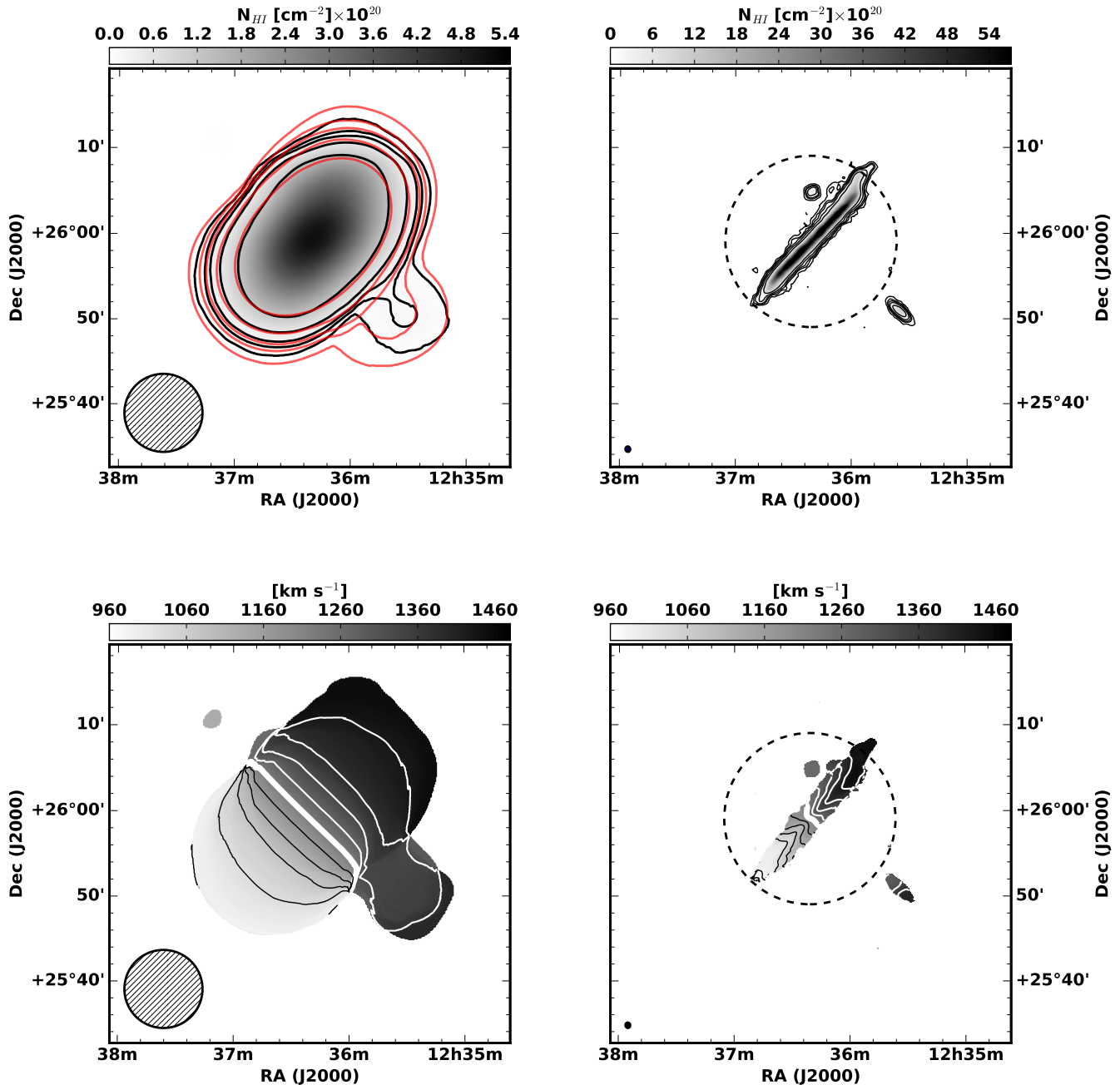


**Figure 12.**  $N_{HI}$  images (top) and velocity fields (bottom) for GBT (left) and WSRT (right) data for NGC4565. The red and black contours in the low resolution  $N_{HI}$  images respectively denote WSRT and GBT data. The contours start at a column density value of  $5 \times 10^{18}$  and continue at 3, 5, 10, and, 25 times that level in the GBT image. The contours in the associated high-resolution WSRT image begin at a level equivalent to  $2.0 \times 10^{19} \text{ cm}^{-2}$  and continue at 3, 5, 10, and 25 times that level. The contours in both velocity fields begin at  $970 \text{ km s}^{-1}$  and continue in steps of  $50 \text{ km s}^{-1}$ . The systemic velocity of  $1230 \text{ km s}^{-1}$  is represented by the thick line, and the approaching and receding velocities are denoted by black and white contours, respectively. The dashed circles in the right-hand panels represent the maximum recoverable angular scales of the WSRT data.

NGC4565 is a large, edge-on SAb galaxy with two very nearby companion galaxies: IC 3571 directly to the north and NGC 4562 to the southwest; only NGC 4562 is partially resolved in our GBT data. The apparent connection is due to the beam confusion stemming from the large GBT beam. The SFR for NGC4565 is among the lowest in the entire HALOGAS sample at  $0.67 M_{\odot} \text{ yr}^{-1}$ . The  $N_{HI}$  images and velocity fields derived from both the GBT and WSRT data sets are detailed in Figure 12. These specific HALOGAS obser-

vations for NGC4565 have been discussed by Zschaechner et al. (2012) and expose a potential interaction between IC3571 and NGC4565 as evidenced by the possible tidal material shown as a separate cloud complex between IC3571 and the disk of NGC4565 in the top right panel of Figure 12. It remains unclear if this structure is related to tidal interactions between the main disk of NGC4565 and IC3571, or an accretion process.

The total HI measured in the GBT data over the same angular region as the WSRT data (including compan-

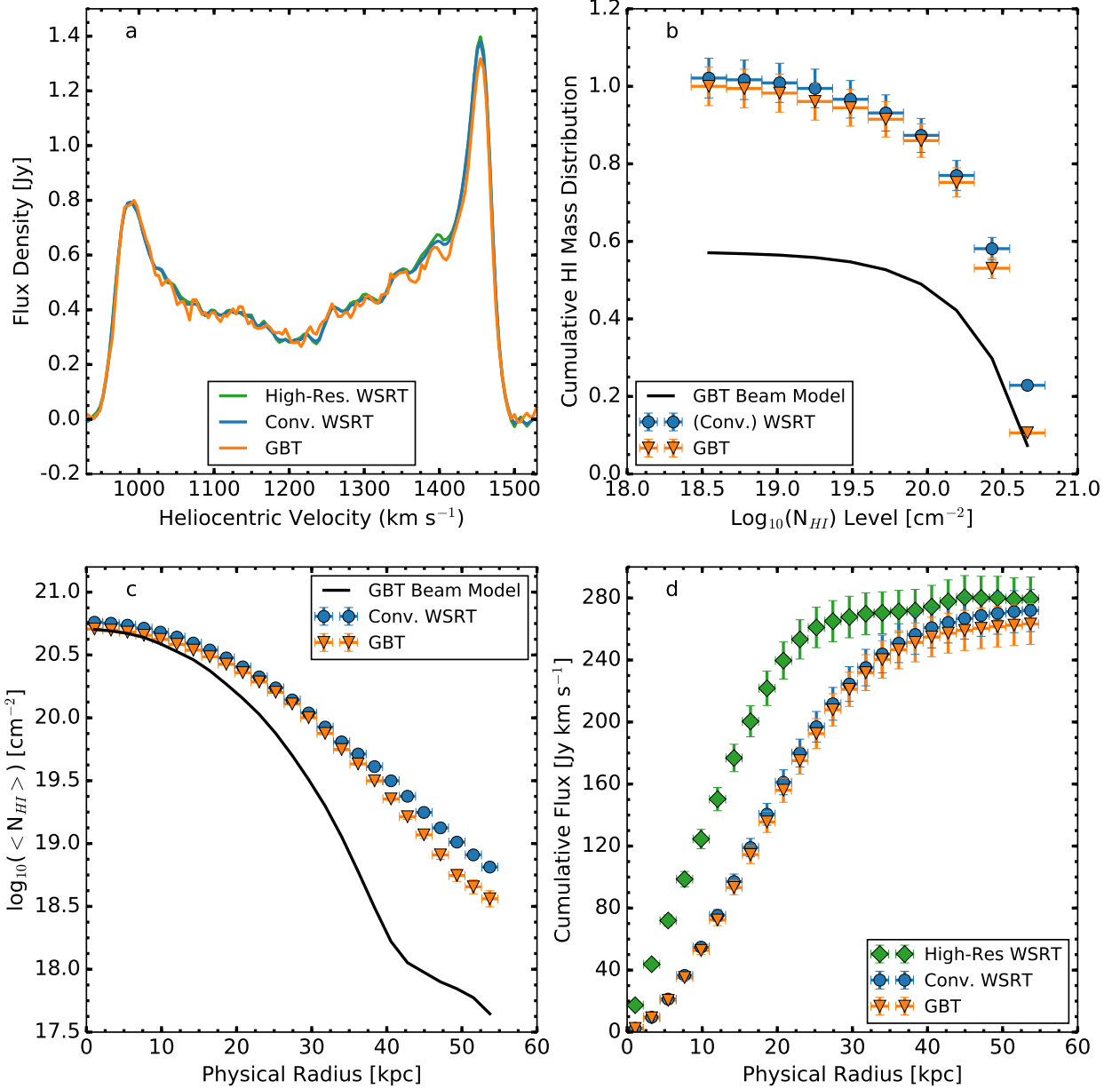


**Figure 13.** Comparison between the high-resolution (green diamonds) WSRT, convolved WSRT (blue circles), and regridded GBT (orange inverted triangles) for NGC4565. *a*: global HI profile; *b*: Cumulative HI mass as a function of  $N_{HI}$ . The dashed and solid black lines simulate the contribution of a Gaussian beam and our GBT beam model, respectively; *c*: projected physical radial dependence on the azimuthally averaged  $N_{HI}$ ; *d*: projected radial dependence of the cumulative flux. In this case, we also show the results of our analysis on the high-resolution WSRT data.



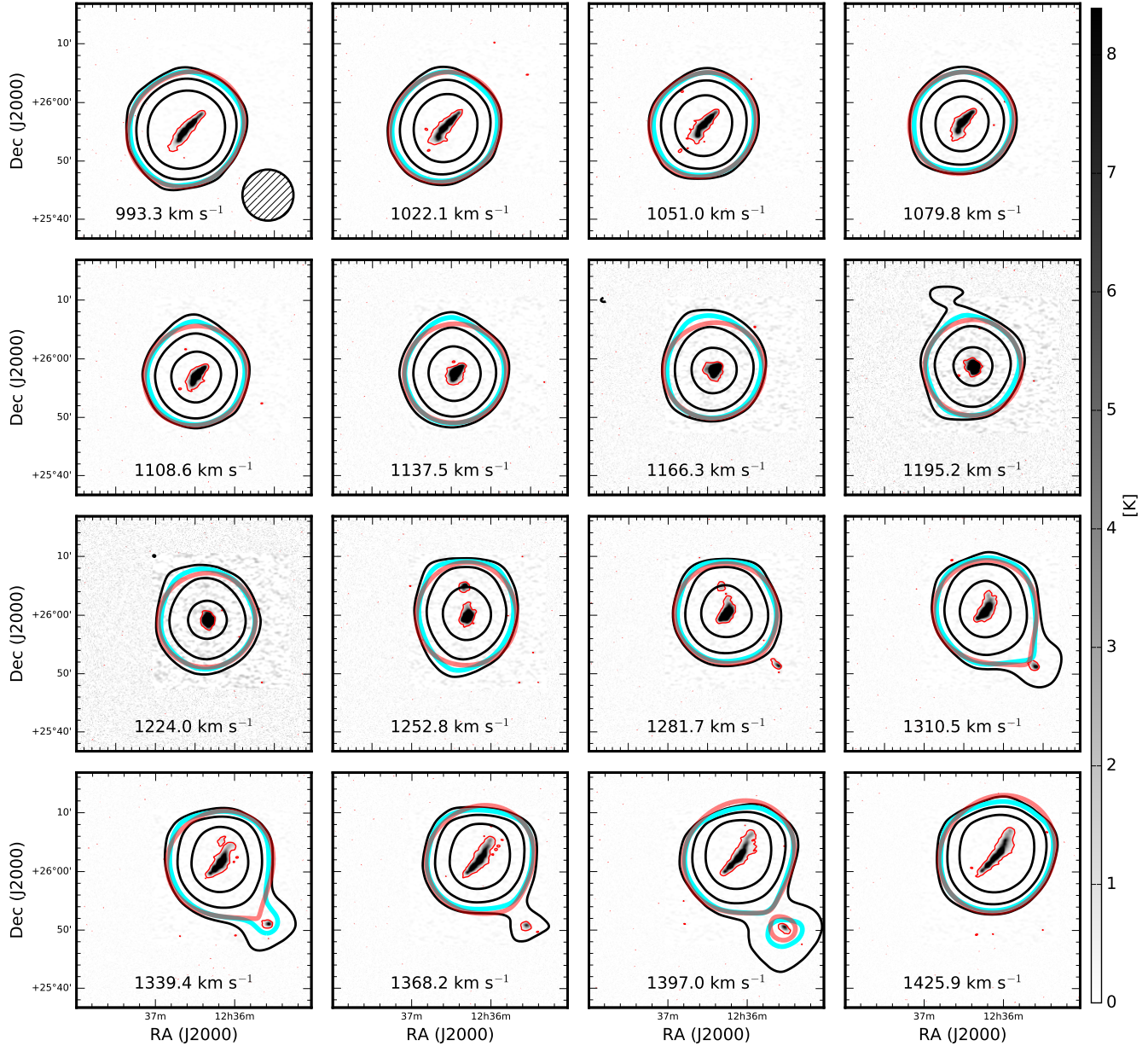


**Figure 14.** Selected channel maps of the NGC4565 WSRT data cube with corresponding GBT channel maps superimposed. The GBT data are shown in black and cyan contours at levels of -3 (dashed), 3, 5 (thick cyan), and 25 times 0.01 K, or equivalently a column density level of  $1.12 \times 10^{17} \text{ cm}^{-2}$  per  $4.12 \text{ km s}^{-1}$  velocity channel. The grey-scale shows the HI emission from the WSRT cube. The thin red line denotes a brightness temperature of 0.54 K, or a column density levels at  $4.05 \times 10^{18} \text{ cm}^{-2}$ , and the thick red line denotes emission at  $5.60 \times 10^{17} \text{ cm}^{-2}$  (the same level of the cyan contour) in the primary-beam corrected WSRT cube convolved down to the GBT resolution. The GBT beam is shown in the top left panel.



ions) is  $(7.46 \pm 0.39) \times 10^9 M_\odot$ , while the primary-beam corrected WSRT data convolved to the GBT resolution gives  $(7.32 \pm 0.37) \times 10^9 M_\odot$ . The HI profiles are shown in Figure 13 and match extremely well.

The cumulative HI mass as a function of  $N_{HI}$  for NGC4565 is presented in Figure 13b. Both distributions also trace each other remarkably well within statistical uncertainties. Additionally, the excellent agreement between all NGC4565 data sets extend to the mean radial column density/cumulative flux. The slight offsets towards higher projected physical radii can be attributed to a residual baseline structure in the GBT cube.

Selected channels are shown in Figure 14 with the GBT and WSRT superimposed on the high-resolution WSRT channels. The  $5\sigma$  level of emission detected from the GBT is consistent with the same level in the convolved WSRT data.

The consistency in the various profiles of Figure 13 and contours in Figure 14 indicate there is no extended diffuse HI reservoir around NGC4565 at the  $N_{HI}$  levels of  $\sim 10^{18} \text{ cm}^{-2}$ . Zschaechner et al. (2012) also did not find evidence using the same high resolution WSRT data of any significant amount of extraplanar HI. The authors of that study proposed this absence is due to no significant disk-halo cycling of material in NGC4565. The lack of any sort of extended low column density HI component supports this conclusion.

## 5. DISCUSSION

In this section we will first discuss our initial survey results in the context of future HI surveys planned for forthcoming radio telescopes. The second subsection explores methods to link the diffuse environment of the HALOGAS galaxies to intrinsic galaxy properties and thus the theoretical predictions from simulations.

### 5.1. Implications for Future HI Surveys

It is well known through a combination of models (e.g., Maloney 1993; Dove & Shull 1994; Bland-Hawthorn et al. 2017) and observations (van Gorkom 1996) that the transition from optically-thick to optically-thin medium decreases the efficiency of self-shielding leading to a dramatic drop in the fraction of HI to total hydrogen (i.e., neutral fraction) primarily due to UV and X-Ray background radiation. This effect is demonstrated in cosmological simulations of the HI distribution (e.g., Popping et al. 2009; Rahmati et al. 2015; Marinacci et al. 2017); in particular, Popping et al. (2009) shows the neutral fraction drops from unity to about a percent between  $18.0 < \log_{10}(N_{HI}/\text{cm}^2) < 20.0$ . This rapid decrease results in a plateau in the HI distribution function that effectively predicts the probability of detecting substantial HI structures at  $N_{HI} \sim 10^{18} \text{ cm}^{-2}$  is very low even with deep surveys. The flux as a function of velocity, cumulative HI mass as a function of  $N_{HI}$ , and azimuthally averaged profiles of column density and cumulative flux show that, overall, the WSRT observations do an excellent job of recovering the low level HI. Save for NGC4414, we see that the HI distributions do not significantly differ between  $N_{HI} \sim 10^{18} \text{ cm}^{-2}$  and  $\sim 10^{19} \text{ cm}^{-2}$ .

The dearth of diffuse HI around these sources has intriguing implications on both the search for cold flow accretion and the determination of the edge of disk gas in late-type galaxies. Many simulations (e.g., Kereš et al.

2005, 2009; Birnboim & Dekel 2003) have predicted that less massive galaxies at low redshift will replenish gas through the form of cold filaments which penetrate the halo down to the disk edge where some fraction of the gas should cool sufficiently to be neutral. Aside from characterizing gas accretion mechanisms, deep HI observations are also useful for tracing large-scale structure in the local Universe. Simulations undertaken by Nuza et al. (2014) predict M31 and Milky Way analogues to sit within a clumpy, yet very diffuse neutral component with HI masses on the order of  $\sim 10^8 M_\odot$  existing predominantly above  $N_{HI} \sim 10^{17} \text{ cm}^{-2}$ . Our cumulative HI mass as a function of  $N_{HI}$  plots are consistent with this prediction. On average, only 2% of the total HI mass exists in column densities below  $1 \times 10^{19} \text{ cm}^{-2}$  as measured in the low-resolution data sets (see Section 5.2). Given the results of Popping et al. (2009), in which the HI surface area distribution function is predicted to steepen at  $N_{HI}$  levels lower than  $10^{18} \text{ cm}^{-2}$ , we expect the offset between the GBT and WSRT cumulative HI distributions would widen considerably with the detection of diffuse HI that traces the large scale structure of the cosmic web, an extended reservoir of diffuse neutral HI, and/or cold flow filaments at the  $10^{18} \text{ cm}^{-2}$  column density level. Such structures would likely be resolved out in an interferometric data set and therefore not contribute at all to the cumulative HI mass at these low  $N_{HI}$  levels.

Detailed analysis of the high-resolution HALOGAS HI data by E. Jütte (2018; in preparation) reveal only a few newly detected HI clouds which may be accreting. Furthermore, maps produced by Wolfe et al. (2016) of the apparent connection between M31 and M33 original discovered by Braun & Thilker (2004), which go several times deeper in column density than our observations, reveal only discrete clouds of HI with masses on the order of  $\sim 10^5 M_\odot$  as opposed to a continuous, smooth diffuse component. These early high-resolution results coupled with the small amount of newly detected HI in the initial GBT data suggest that, if these galaxies are currently accreting gas, most of it must be ionized and unobservable in HI emission. The absence of significant HI structure at the  $N_{HI}$  level of  $10^{18} \text{ cm}^{-2}$  supports the notion that HI surveys of external galaxies must go *at least* as deep as  $N_{HI} \sim 10^{17} \text{ cm}^{-2}$  to substantially increase the probability of detecting emission associated with the IGM and/or cold mode accretion.

### 5.2. The Relationship Between Diffuse HI and Cold Mode Accretion

While the GBT data do not reveal new features below the  $N_{HI} \sim 10^{18} \text{ cm}^{-2}$  level, as the remaining data are analyzed it is still important to consider the implications of potential diffuse features and their relation to cold flows as predicted from simulations. Namely, how would diffuse HI related to cold mode accretion manifest itself in emission? Does the diffuse gas originate from outflows, tidal interactions with nearby companions, or accretion from the IGM?

To explore the relationship between the diffuse HI around nearby galaxies and simulation predictions, we measure the diffuse HI mass fraction as defined by

$$f_{19} = 1 - \frac{M_{19}}{M_{HI}}, \quad (9)$$

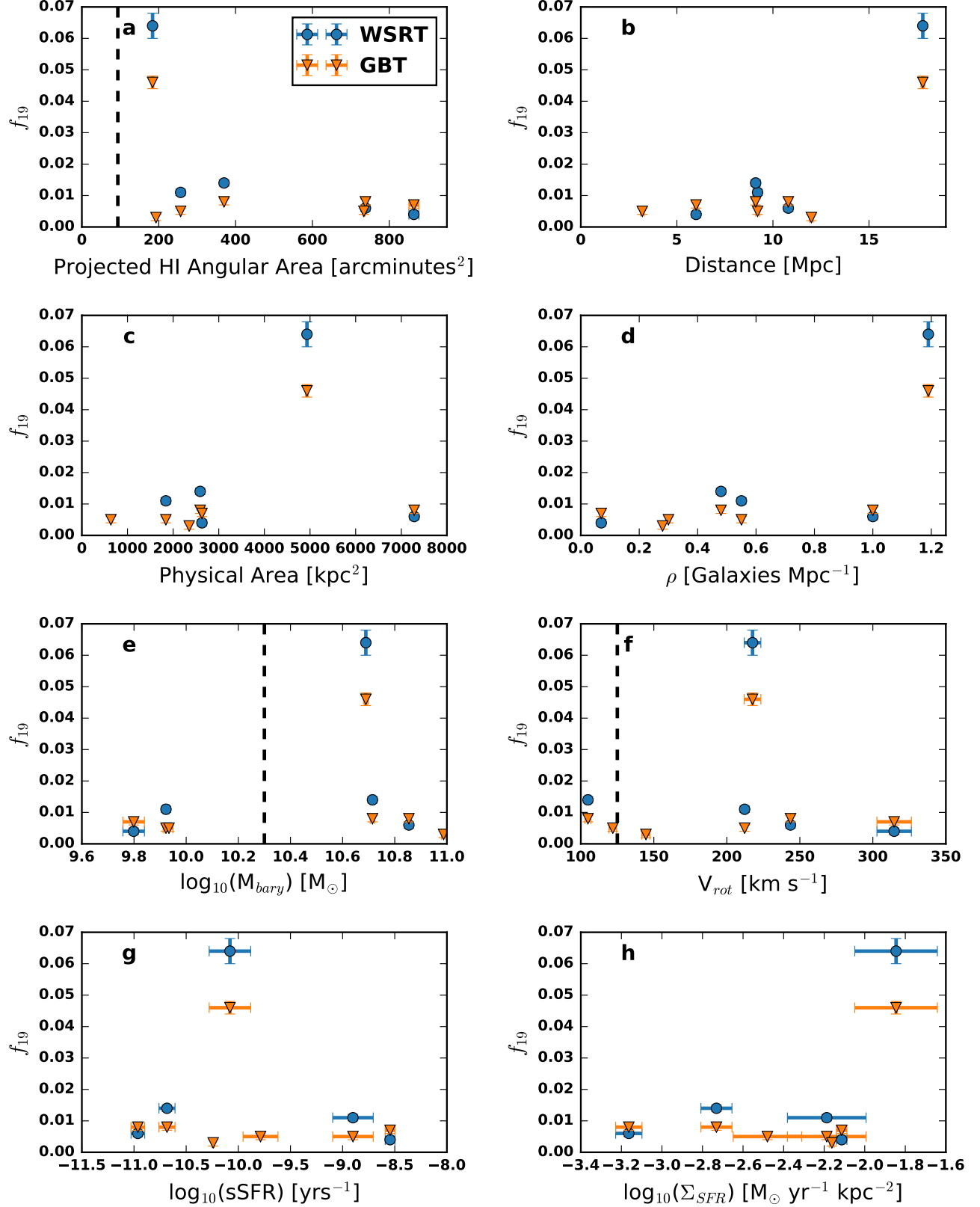


**Figure 15.** Environmental and intrinsic property relations with excess HI ratio,  $f_{19}$ . a:  $f_{19}$  as a function of projected angular area. The vertical dashed line marks the area of the GBT beam (up to the FWHM); b:  $f_{19}$  as a function of distance; c:  $f_{19}$  as a function of projected physical area; d:  $f_{19}$  as a function of galaxy density.  $\rho$  is taken from Tully (1988); e:  $f_{19}$  as a function of the source galaxy baryonic mass ( $M_{\text{HI}} + M_{\star}$ ). The vertical dashed line corresponds to the baryonic mass threshold from Kereš et al. (2005) below which cold mode accretion is the dominant accretion mechanism; f:  $f_{19}$  as a function of rotational velocity. The vertical dashed line corresponds to the threshold mass at which galaxies should be gas dominated (Kannappan et al. 2013); g:  $f_{19}$  as a function of specific SFR (sSFR); h:  $f_{19}$  as a function of the surface density of star formation ( $\Sigma_{\text{SFR}}$ ).

where  $M_{HI}$  is the total HI mass detected for that particular telescope (taken from pixels with  $N_{HI}$  values at and above the  $3\sigma$  detection limit listed in Table 2 to avoid measuring into the noise) and  $M_{19}$  is the HI mass above the  $N_{HI}$  level of  $1 \times 10^{19} \text{ cm}^{-2}$  in the unmasked GBT and convolved WSRT  $N_{HI}$  images.

The purpose of this parameter is to measure the mass fraction of diffuse HI associated with a given galaxy. We can then relate the presence (or dearth) of diffuse HI to properties predicted by cosmological simulations to correlate with higher rates of cold mode accretion. In the context of our subsequent discussion, we define diffuse HI to firstly be below the  $N_{HI}$  level of  $1 \times 10^{19} \text{ cm}^{-2}$ , which is on the same order as the analytical critical column densities derived by Bland-Hawthorn et al. (2017), Maloney (1993), and Dove & Shull (1994) (i.e., where the HI transitions from mostly neutral to mostly ionized) and is approximately the  $5\sigma$   $N_{HI}$  detection limit of the native resolution WSRT data over a  $20 \text{ km s}^{-1}$  line. Secondly, diffuse HI is implied to be extended over angular scales larger than the maximum recoverable angular scale of the WSRT ( $\sim 20'$ ). A lower  $f_{19}$  value measured for a well-resolved source (relative to the larger GBT beam) would therefore demonstrate that most of the HI resides at higher column densities, indicating no signs of a diffuse inflowing component that can be observed in emission. On the other hand, a higher  $f_{19}$  value would suggest the WSRT resolves out large scale HI features that possess  $N_{HI}$  levels lower than  $\sim 10^{19} \text{ cm}^{-2}$ .

Because  $N_{HI}$  is directly proportional to the measured brightness temperature, which is itself averaged over the beam solid angle, the usefulness of the  $f_{19}$  parameter to characterize the diffuse HI mass fraction relies on the sources being well-resolved. Once the source becomes unresolved, our measurement — that is effectively the convolution of the true HI emission distribution with the larger beam — will spread the flux of the out to angular scales where the beam response is lower, thus measuring low column density values that are no longer physical but still nevertheless begin to dominate the overall HI mass fraction and bias our quantity. While  $f_{19}$  provides a quantity that can be related to properties predicted to be influential to accretion, given that the sources presented in this work are at different distances, span a range of physical scales, and are in general inhomogeneous, acute attention to several resolution indicators, which will be discussed below, is required to ensure a  $f_{19}$  value for a given galaxy is not biased by resolution effects.

The  $f_{19}$  values are summarized in Table 3. In general, the  $f_{19}$  values derived from the convolved WSRT data are similar to their regridded GBT counterparts. In the cases where the convolved WSRT values are higher, the increase can be attributed to the increased column density sensitivity when the WSRT data (where emission fills the synthesized beam) is convolved to low resolution. In addition to the four sources discussed above, we also compute  $f_{19}$  for three galaxies which have similar GBT data: NGC2403 (also a HALOGAS source) (Fraternali et al. 2001, 2002; de Blok et al. 2014), NGC2997 (Pisano 2014), and NGC6946 (with additional deep WSRT data; Pisano 2014; Boomsma et al. 2008).

Our initial small sample size inhibits us from making any significant conclusions about the relations between

fraction of diffuse HI and any of the properties which trace simulation predictions. However, investigating the trends within our initial small sample will provide intuition on any underlying correlations that may be revealed as we build up our sample and flesh out issues due to resolution effects.

As mentioned above, it is critical to rule out observational or resolution bias as a source for potential trends. Figure 15a plots  $f_{19}$  for each source as a function of projected HI angular area computed from the number of pixels above the associated  $2\sigma$   $N_{HI}$  level from Table 2 in the unmasked high-resolution WSRT  $N_{HI}$  images. Note that in each panel the blue circles denote  $f_{19}$  values derived from convolved WSRT data and the orange inverted triangles represent GBT  $f_{19}$  values. The vertical dashed line represents the area of the GBT beam above which extended source structure becomes resolved. While it is encouraging to see all of the projected HI angular area data points fall to the right of the GBT beam area, this is only one indication that our  $f_{19}$  parameter is not biased by resolution effects. Because  $f_{19}$  is essentially one minus the ratio of the integral of the cumulative HI mass distribution taken from bins larger than  $Ll_{g10}(N_{HI}/\text{cm}^2) = 19.0$  to an integral taken over the full range of  $N_{HI}$  bins, a better indicator for possible resolution bias is to ensure the data points of the cumulative HI mass distribution for a given source do not trace the simulated unresolved observation (i.e., the GBT beam profile).

In the case of Figure 15a, the highest  $f_{19}$  value is indeed associated with NGC4414, whose angular area is only a few times that of the GBT beam. Figure 10b shows the WRST data cumulative HI mass fraction is consistent with the observation of an unresolved source within the large GBT beam at higher  $N_{HI}$  bins, while the GBT cumulative HI mass distribution shows only marginal improvement over the simulated unresolved observation. The slight trend between increasing distance and increasing  $f_{19}$  values in Figure 15b does hint that  $f_{19}$  will be influenced by the large GBT beam. The high  $f_{19}$  values in both data sets for NGC4414 reveal how the effects of resolution can bias the calculation of  $f_{19}$ . That said, we also see sources with comparable  $f_{19}$  values over a large range of projected angular areas whose cumulative HI mass functions do not trace a simulated observation of an unresolved source. Figures 15a and b therefore demonstrate that  $f_{19}$  is not generally biased when applied to well-resolved sources.

The physical extent of a diffuse gas reservoir should ideally scale with a diffuse HI mass fraction. Plotting  $f_{19}$  as a function of physical projected HI area in Figure 15c shows that the highest  $f_{19}$  value is associated with the second largest physical extent; however, the high  $f_{19}$  value is very likely biased due to the greater distance of the source. On the other hand, the second highest  $f_{19}$  value corresponds to the very well-resolved galaxy of NGC4565, demonstrating the expected scaling. That said, the fact this particular GBT  $f_{19}$  value is the second highest value of the sample by only about a factor of two underscores the lack of a significant diffuse HI around NGC4565.

A relationship between  $f_{19}$  and galaxy properties investigated in simulations (e.g., Kereš et al. 2005, 2009) should give some indication as to whether any newly probed diffuse component could be related to accretion

from the IGM. For example, simulations show cold mode accretion is still an available channel for gas accretion around nearby galaxies with relatively low halo masses ( $M_{halo} \leq 10^{11.4} M_{\odot}$ ) and in low density environments. Any trend between excess HI and properties known to be responsible for the presence of excess HI could provide observational evidence, albeit indirect, that the observed excess HI is being accreted directly from the IGM. Figure 15d plots  $f_{19}$  as a function of galaxy density, or the number of galaxies per  $\text{Mpc}^{-3}$  ( $\rho$ ); we estimate  $\rho$  by using values derived in Tully (1988). Any correlation between  $f_{19}$  and  $\rho$  should provide insight into the influence of tidal forces. No obvious trend presents itself here. The absence of a trend in the context of the full sample would be indicative of the relative unimportance of tidal interactions as compared to outflows or accretion to the presence of extraplanar and/or an extended gas reservoir.

Figure 15e plots  $f_{19}$  as a function of the baryonic mass ( $M_{bary}$ ) where the vertical dashed lines represent the threshold set by the simulations of Kereš et al. (2005) where cold mode accretion is predicted to be the dominant mechanism of gas accretion. Assuming the dust and molecular gas components to be negligible to the total gas mass, we calculate  $M_{bary}$  to be equal to  $M_{HI} \cdot 1.36 + M_*$ , where  $M_{HI}$  is measured by the GBT. The factor of 1.36 in the leading term corrects for the fraction of neutral He. There is no apparent trend between  $f_{19}$  and  $M_{bary}$ . Additionally, Figure 15f presents the relationships between  $f_{19}$  and rotational velocity ( $V_{rot}$ ). The dashed line in this plot shows the observational threshold such that galaxies with  $V_{rot} \leq 125 \text{ km s}^{-1}$  are expected to be gas dominated due to continuous sustained growth (Kannappan 2004; Kannappan et al. 2013). Again, no discernible trend is observed.

The final origin scenario for a large diffuse component in these galaxies is related to outflows due to star formation activity in the disk. The relationship between  $f_{19}$  and specific star formation rate (sSFR), which is the star formation rate per unit stellar mass, is presented in Figure 15g;  $f_{19}$  as a function of the surface density of star formation is shown in Figure 15h. We derive the surface density of star formation by dividing the SFR by the de-projected physical area. We compute the physical area assuming each galaxy face-on is roughly circular and utilize the de-projected and extinction corrected semimajor angular diameter computed from the B-band 25 mag arcsec $^{-2}$  isophote (de Vaucouleurs et al. 1976). Excluding the rightmost data points in Panel h (which may, at some level, be biased by resolution), there is no indication of trend between increasing  $f_{19}$  with increased star formation activity. A positive correlation suggests more energy per gravitational potential in such galaxies, which points to the possible existence of outflows.

Some, if not most, of the extraplanar gas observed around nearby galaxies must originate from outflows described by galactic fountain (Bregman 1980; Norman & Ikeuchi 1989; Fraternali 2017), and are driven by the injection of momentum and energy into the local interstellar medium from supernovae. In most cases, such outflows are the more feasible origin for diffuse HI in the form of extraplanar gas. Fraternali & Binney (2006) and Fraternali & Binney (2008) outline dynamical models that accurately reproduce the general vertical distri-

bution of gas in NGC891 and NGC2403 with a necessary energy injection of only <4% of the energy released by supernovae. But while the general distribution is reproduced, the rotational velocity of the model halos is much too high compared to observations. The discrepancy between modeled and observed rotational velocities suggested the acquisition of low-angular momentum gas from the IGM in order to slow the model halos. More recently, however, Marinacci et al. (2010) and Fraternali (2017) show that including the effects of condensation, drag (ram pressure), and radiative cooling in these ballistic models of fountain gas will prevent momentum loss in the cold gas while also increasing the transfer of momentum to intermediate temperature material as opposed to the hot coronal gas. The increase in rotational velocity is therefore mitigated, thus bringing these models into agreement with observational data. By incorporating radiative cooling of the hot coronal gas, it can condense in the wake of fountain clouds which consequently raises the accretion rate of low-metallicity gas onto the central disk of an embedded galaxy. Specifically, Fraternali (2017) recover cold gas accretion rates comparable with the the SFR of NGC891 and NGC2403.

We end this section by posturing what type of observational constraints between  $f_{19}$  and the inherent galaxy properties shown in Figure 15 would indicate the possibility of observing active cold mode accretion. The first necessity would be a  $f_{19}$  value from the GBT data that is well above the WSRT and well to the right of the vertical dashed line in Figure 15a. This would indicate that the WSRT had resolved out significantly extended structure and physical column densities as the emission has filled the large GBT beam. That same large  $f_{19}$  GBT data point would then need to be associated with a small  $\rho$  to indicate isolation and that tidal interactions are not likely to be the origin of the diffuse environment. We would next need to see the  $f_{19}$  value fall below the  $M_{bary}$  and  $V_{rot}$  thresholds to ensure the galaxy is consistent with the predictions of the cosmological simulations. Finally, the presence of a significant diffuse HI component would need to be associated with a relatively insignificant amount of star formation activity ruling out the presence of substantial outflows and subsequent condensation from the fountain activity.

The derived properties of these four sources are summarized in Table 3. The columns are (1) Source Name; (2) HI mass measured in the GBT data; (3) HI mass measured in the convolved WSRT data; (4) HI mass as measured in the high-resolution WSRT data; (5) stellar mass derived from the *WISE* All Sky Image Atlas; (6) baryonic mass; (7) deprojected physical area; (8) rotation velocity from HYPERLEDA (9)  $f_{19}$  measured in the convolved WSRT cube; and (10)  $f_{19}$  measured in the GBT cube. The relationships in this section should be considered diagnostic in that we are trying to develop intuition into what trends should exist in galaxies that are actively undergoing cold mode accretion. The low number of sources studied in this work inhibit any conclusions. We will continue to build our statistical sample with future analysis of the HALOGAS, THINGS, and ultimately the *MeerKAT HI Observations of Nearby Galactic Objects: Observing Southern Emitters* (MHONGOOSE; de Blok et al. 2017) and the *Imaging Galaxies Inter-galactic and Nearby Environment* (IMAGINE) galaxy samples

in order to search for correlations between the presence of a significant diffuse HI environment and the intrinsic galaxy properties which should trace accretion from the IGM in the local Universe.

## 6. CONCLUSIONS AND FUTURE WORK

We presented an initial analysis of deep ( $N_{HI} \sim 10^{18} \text{ cm}^{-2}$ ) GBT observations of four sources (NGC891, NGC925, NGC4414, and NGC4565) out of 24 total sources in the HALOGAS survey. These observations are among the most sensitive HI observations of external galaxies to date. In order to directly compare interferometer and single dish data, we solve for an optimal smoothing kernel specific to each source and convolve the WST data to GBT angular resolution. Our main conclusions are:

- As we do not find significant spatially extended HI features, we conclude that the WSRT data do an excellent job recovering the diffuse ( $18 \leq \log_{10}(N_{HI}) \leq 19$ ) HI around these four sources. In the case of NGC925, we detect about 20% more HI than observations done with the VLA as part of the THINGS survey. The discrepancy is likely due in large part to the increased surface brightness sensitivity of the WSRT data since the ability to detect extended structure between the two surveys is very similar. The excellent agreement between the global HI profiles, cumulative HI mass as a function of  $N_{HI}$ , radial mean column density profiles, and radial cumulative flux for the GBT and convolved WSRT data provides additional evidence in support of this conclusion.
- The cumulative HI mass as a function of HI column density reveals the diffuse HI associated with these galaxies does not change significantly over the range  $\log_{10}(N_{HI}/\text{cm}^{-2}) = 18.0$  to  $\log_{10}(N_{HI}/\text{cm}^{-2}) = 19.5$ . The flat behavior is consistent with predictions from simulations, which show the neutral fraction is around 1% at  $\log_{10}(N_{HI}/\text{cm}^{-2}) = 18.0$ . Scaling our GBT beam model to the peak column density of the GBT data and repeating our analysis to essentially simulate an unresolved source produces a similarly flat distribution, which suggests the lowest column density bins include some values that trace the extended structure of the GBT beam. That said, there is generally a moderate offset between the data and model cumulative HI mass distributions. The overall agreement between the GBT and WSRT data sets, if extended to the other sources in our survey, suggests future surveys must probe column densities at the  $\sim 10^{17} \text{ cm}^{-2}$  level to increase the probability of detecting HI associated with cosmic web structure or possibly cold-mode accretion.
- We define a parameter,  $f_{19}$ , equal to one minus the ratio between the HI mass measured at and above  $\log_{10}(N_{HI}) = 19$  and the source's total HI mass. We find that, on average (and excluding data that may suffer from resolution effects), this value is equal to 2%, indicating the diffuse extended disks of these galaxies do not constitute a significant fraction of the overall mass.

One observational method to differentiate between inflow/outflow origins is a measure of metallicity using UV absorption lines (e.g., S II) utilizing the Cosmic Origins Spectrograph on the *Hubble* Space Telescope. If a significant diffuse HI feature is seen around a source as we analyze the full survey, and a fortuitous background quasar along the line of sight, a metallicity of  $\sim 0.1 Z_{\odot}$  would be highly indicative of a CGM origin.

To establish or rule out cold mode accretion as a feasible avenue for nearby galaxies to refuel their gas content, we must continue to analyze galaxies within the HALOGAS sample that satisfy the mass constraints set by simulations, show large diffuse HI mass fractions and low SFRs, and reside in low density environments. Due to our small sample size we can only present foundational work to uncover any underlying correlations between large mass fractions of diffuse HI and galaxy properties. Future work will focus on the analysis techniques presented here in order investigate the origins of these large HI filaments, apply short spacing corrections to the WSRT data, and continue the investigation into role of HI in galaxy evolution.

We thank Richard Prestage and Jay Lockman for insightful discussions on the behavior and geometry of the innermost sidelobes of the GBT. We are also grateful to Filippo Fraternali for his helpful discussions on the caveats of convolving high-resolution data and interpretation of residual emission. Finally, we thank the anonymous referee for their constructive comments that helped to focus the analysis and conclusions presented in this work. This study was funded by the NSF CAREER grant AST-1149491. The National Radio Astronomy Observatory is a facility of the National Science Foundation operated under cooperative agreement by Associated Universities, Inc. T. H. J. acknowledges financial support from the National Research Foundation (NRF; South Africa).

## REFERENCES

- Aniano, G., Draine, B. T., Gordon, K. D., & Sandstrom, K. 2011, *PASP*, 123, 1218
- Bekki, K. 2008, *MNRAS*, 390, L24
- Benjamin, R. A. 2002, in *Astronomical Society of the Pacific Conference Series*, Vol. 276, *Seeing Through the Dust: The Detection of HI and the Exploration of the ISM in Galaxies*, ed. A. R. Taylor, T. L. Landecker, & A. G. Willis, 201
- Birnboim, Y., & Dekel, A. 2003, *MNRAS*, 345, 349
- Bland-Hawthorn, J., Maloney, P. R., Stephens, A., Zovaro, A., & Popping, A. 2017, *ApJ*, 849, 51
- Boomsma, R., Oosterloo, T. A., Fraternali, F., van der Hulst, J. M., & Sancisi, R. 2008, *A&A*, 490, 555
- Boothroyd, A. I., Blagrove, K., Lockman, F. J., et al. 2011, *A&A*, 536, A81
- Braun, R., & Thilker, D. 2004, in *Astronomical Society of the Pacific Conference Series*, Vol. 327, *Satellites and Tidal Streams*, ed. F. Prada, D. Martinez Delgado, & T. J. Mahoney, 139
- Braun, R., & Walterbos, R. A. M. 1985, *A&A*, 143, 307
- Bregman, J. N. 1980, *ApJ*, 236, 577
- Buat, V., Boissier, S., Burgarella, D., et al. 2008, *A&A*, 483, 107
- Buat, V., Giovannoli, E., Heinis, S., et al. 2011, *A&A*, 533, A93
- Chynoweth, K. M., Langston, G. I., & Holley-Bockelmann, K. 2011, *AJ*, 141, 9
- Cluver, M. E., Jarrett, T. H., Hopkins, A. M., et al. 2014, *ApJ*, 782, 90
- Corbelli, E., Lorenzoni, S., Walterbos, R., Braun, R., & Thilker, D. 2010, *A&A*, 511, A89

Derived Properties	NGC891	NGC925	NGC2403	NGC2997	NGC4414	NGC4565	NGC6946
GBT HI Mass [ $10^9 M_\odot$ ]	3.86±0.19	5.79±0.29	3.39±0.37	7.0±1.0	5.43±0.27	7.33±0.37	3.80±0.69
Conv. WSRT HI Mass [ $10^9 M_\odot$ ]	3.81±0.19	5.54±0.28	—	—	4.56±0.22	7.46±0.39	—
High-Res. WSRT HI Mass [ $10^9 M_\odot$ ]	3.90±0.18	5.57±0.28	—	—	4.63±0.23	7.55±0.38	—
$M_*$ [ $10^{10} M_\odot$ ]	0.30±0.10	4.40±0.10	0.39±0.01	8.70±0.10	4.15±0.10	6.15±0.10	0.12±0.01
$M_{\text{barry}}$ [ $10^{10} M_\odot$ ]	0.82±0.02	5.20±0.10	0.86±0.03	9.71±0.18	4.89±0.10	7.15±0.10	6.29±0.59
Deprojected Physical Area [ $\text{kpc}^2$ ]	603±6	490±6	122±3	726±11	241±24	976±10	416±3
$V_{\text{rot}}^{\text{a}}$ [ $\text{km s}^{-1}$ ]	212±2	105±2	196±1	145±3	218±6	244	315±12
WSRT $f_{19}$	0.011±0.001	0.014±0.001	—	—	0.064±0.004	0.006±0.001	0.004±0.001
GBT $f_{19}$	0.005±0.001	0.008±0.001	0.005±0.001	0.003±0.001	0.046±0.002	0.008±0.001	0.003±0.001

**Table 3**  
Summary of Derived Properties

<sup>a</sup>Rotation velocity taken from *HYPERLEDA* search

- de Blok, W. J. G., Józsa, G. I. G., Patterson, M., et al. 2014, *A&A*, 566, A80
- de Blok, W. J. G., Adams, E. A. K., Amram, P., et al. 2017, ArXiv e-prints, arXiv:1709.08458
- de Vaucouleurs, G., de Vaucouleurs, A., & Corwin, J. R. 1976, in Second reference catalogue of bright galaxies, Vol. 1976, p. Austin: University of Texas Press., Vol. 1976
- Dove, J. B., & Shull, J. M. 1994, *ApJ*, 423, 196
- Driver, S. P., Norberg, P., Baldry, I. K., et al. 2009, *Astronomy and Geophysics*, 50, 5.12
- Driver, S. P., Hill, D. T., Kelvin, L. S., et al. 2011, *MNRAS*, 413, 971
- Fraternali, F. 2017, in *Astrophysics and Space Science Library*, Vol. 430, Gas Accretion onto Galaxies, ed. A. Fox & R. Davé, 323
- Fraternali, F., & Binney, J. J. 2006, *MNRAS*, 366, 449
- . 2008, *MNRAS*, 386, 935
- Fraternali, F., Marasco, A., Armillotta, L., & Marinacci, F. 2015, *MNRAS*, 447, L70
- Fraternali, F., Oosterloo, T., Sancisi, R., & van Moorsel, G. 2001, *ApJL*, 562, L47
- Fraternali, F., van Moorsel, G., Sancisi, R., & Oosterloo, T. 2002, *AJ*, 123, 3124
- Gil de Paz, A., Boissier, S., Madore, B. F., et al. 2007, *ApJS*, 173, 185
- Gottesman, S. T. 1980, *AJ*, 85, 824
- Heald, G., Józsa, G., Serra, P., et al. 2011, *A&A*, 526, A118
- . 2012, *A&A*, 544, C1
- Jarrett, T. H., Masci, F., Tsai, C. W., et al. 2013, *AJ*, 145, 6
- Jorsater, S., & van Moorsel, G. A. 1995, *AJ*, 110, 2037
- Joung, M. R., Bryan, G. L., & Putman, M. E. 2012, *ApJ*, 745, 148
- Kannappan, S. J. 2004, *ApJL*, 611, L89
- Kannappan, S. J., Stark, D. V., Eckert, K. D., et al. 2013, *ApJ*, 777, 42
- Karachentsev, I. D., & Kaisina, E. I. 2013, *AJ*, 146, 46
- Kauffmann, G., Li, C., & Heckman, T. M. 2010, *MNRAS*, 409, 491
- Kereš, D., Katz, N., Fardal, M., Davé, R., & Weinberg, D. H. 2009, *MNRAS*, 395, 160
- Kereš, D., Katz, N., Weinberg, D. H., & Davé, R. 2005, *MNRAS*, 363, 2
- Lelli, F., Verheijen, M., & Fraternali, F. 2014, *MNRAS*, 445, 1694
- Madau, P., & Dickinson, M. 2014, *ARA&A*, 52, 415
- Maloney, P. 1993, *ApJ*, 414, 41
- Mangum, J. G., Emerson, D. T., & Greisen, E. W. 2007, *A&A*, 474, 679
- Marinacci, F., Fraternali, F., Ciotti, L., & Nipoti, C. 2010, *MNRAS*, 401, 2451
- Marinacci, F., Grand, R. J. J., Pakmor, R., et al. 2017, *MNRAS*, 466, 3859
- Nelson, D., Vogelsberger, M., Genel, S., et al. 2013, *MNRAS*, 429, 3353
- Norman, C. A., & Ikeuchi, S. 1989, *ApJ*, 345, 372
- Noterdaeme, P., Petitjean, P., Carithers, W. C., et al. 2012, *A&A*, 547, L1
- Nuza, S. E., Parisi, F., Scannapieco, C., et al. 2014, *MNRAS*, 441, 2593
- Oosterloo, T., Fraternali, F., & Sancisi, R. 2007, *AJ*, 134, 1019
- Pisano, D. J. 2014, *AJ*, 147, 48
- Pisano, D. J., Wilcots, E. M., & Elmegreen, B. G. 1998, *AJ*, 115, 975
- Popping, A., Davé, R., Braun, R., & Oppenheimer, B. D. 2009, *A&A*, 504, 15
- Putman, M. E., Peek, J. E. G., Muratov, A., et al. 2009, *ApJ*, 703, 1486
- Rahmati, A., Schaye, J., Bower, R. G., et al. 2015, *MNRAS*, 452, 2034
- Rees, M. J., & Ostriker, J. P. 1977, *MNRAS*, 179, 541
- Ribaldo, J., Lehner, N., Howk, J. C., et al. 2011, *ApJ*, 743, 207
- Richter, P., Nuza, S. E., Fox, A. J., et al. 2017, *A&A*, 607, A48
- Rupen, M. P. 1991, *AJ*, 102, 48
- Sancisi, R., & Allen, R. J. 1979, *A&A*, 74, 73
- Sancisi, R., Fraternali, F., Oosterloo, T., & van der Hulst, T. 2008, *A&A Rev.*, 15, 189
- Sault, R. J., Teuben, P. J., & Wright, M. C. H. 1995, in *Astronomical Society of the Pacific Conference Series*, Vol. 77, *Astronomical Data Analysis Software and Systems IV*, ed. R. A. Shaw, H. E. Payne, & J. J. E. Hayes, 433
- Stanimirovic, S. 2002, in *Astronomical Society of the Pacific Conference Series*, Vol. 278, *Single-Dish Radio Astronomy: Techniques and Applications*, ed. S. Stanimirovic, D. Altschuler, P. Goldsmith, & C. Salter, 375–396
- Stocke, J. T., Keeney, B. A., & Danforth, C. W. 2010, *PASA*, 27, 256
- Swaters, R. A., Sancisi, R., & van der Hulst, J. M. 1997, *ApJ*, 491, 140
- Tully, R. B. 1988, *Nearby galaxies catalog*
- van Gorkom, J. 1996, in *Astronomical Society of the Pacific Conference Series*, Vol. 106, *The Minnesota Lectures on Extragalactic Neutral Hydrogen*, ed. E. D. Skillman, 293
- Verheijen, M. A. W., & Sancisi, R. 2001, *A&A*, 370, 765
- Wakker, B. P., Savage, B. D., Sembach, K. R., et al. 2003, *ApJS*, 146, 1
- Walter, F., Brinks, E., de Blok, W. J. G., et al. 2008, *AJ*, 136, 2563
- Wolfe, S. A., Lockman, F. J., & Pisano, D. J. 2016, *ApJ*, 816, 81
- Wolfe, S. A., Pisano, D. J., & Lockman, F. J. 2015, *GBT Memo Series*, GBT Memo 289
- Wolfe, S. A., Pisano, D. J., Lockman, F. J., McGaugh, S. S., & Shaya, E. J. 2013, *Nature*, 497, 224
- Zhu, Y.-N., Wu, H., Li, H.-N., & Cao, C. 2010, *Research in Astronomy and Astrophysics*, 10, 329
- Zschaechner, L. K., Rand, R. J., Heald, G. H., Gentile, G., & Józsa, G. 2012, *ApJ*, 760, 37